



Programa de Pós-Graduação
GEOCIÊNCIAS



UNIVERSIDADE FEDERAL DO RIO GRANDE DO SUL
INSTITUTO DE GEOCIÊNCIAS
PROGRAMA DE PÓS-GRADUAÇÃO EM GEOCIÊNCIAS

O ELO ENTRE A SERPENTINIZAÇÃO, TRANSPORTE DE SÍLICA, CARBONATOS E SEDIMENTAÇÃO RIFT

YURI DE MELO PORTELLA

ORIENTADOR – Prof. Dr. Rommulo Vieira Conceição

COORIENTADOR – Prof. Dr. Rodrigo Sebastian Iglesias (IPR – PUCRS)

Porto Alegre, 2020



Programa de Pós-Graduação
GEOCIÊNCIAS



**UNIVERSIDADE FEDERAL DO RIO GRANDE DO SUL
INSTITUTO DE GEOCIÊNCIAS
PROGRAMA DE PÓS-GRADUAÇÃO EM GEOCIÊNCIAS**

**O ELO ENTRE A SERPENTINIZAÇÃO, TRANSPORTE DE
SÍLICA, CARBONATOS E SEDIMENTAÇÃO RIFT**

YURI DE MELO PORTELLA

ORIENTADOR – Prof. Dr. Rommulo Vieira Conceição

COORIENTADOR – Prof. Dr. Rodrigo Sebastian Iglesias (IPR – PUCRS)

BANCA EXAMINADORA

Dr. Peter Szatmari – Petróleo Brasileiro S.A. (PETROBRAS)

Profa. Dra. Carla Cristine Porcher – Instituto de Geociências, Universidade Federal do Rio Grande do Sul

Prof. Dr. Stephen Foley - Macquarie University (Australia)

Dissertação de Mestrado
apresentada como requisito
parcial para a obtenção do
Título de Mestre em Ciências.

Porto Alegre, 2020



CIP - Catalogação na Publicação

Portella, Yuri de Melo
O elo entre a serpentinização, transporte de sílica, carbonatos e sedimentação rift / Yuri de Melo Portella. -- 2020.

59 f.
Orientador: Rommulo Vieira Conceição.

Coorientador: Rodrigo Sebastian Iglesias.

Dissertação (Mestrado) -- Universidade Federal do Rio Grande do Sul, Instituto de Geociências, Programa de Pós-Graduação em Geociências, Porto Alegre, BR-RS, 2020.

1. Petrologia Experimental. 2. Serpentinização. 3. Interação rocha-fluido. 4. Silicificação. 5. Pré-sal.
I. Conceição, Rommulo Vieira, orient. II. Iglesias, Rodrigo Sebastian, coorient. III. Título.

Elaborada pelo Sistema de Geração Automática de Ficha Catalográfica da UFRGS com os dados fornecidos pelo(a) autor(a).



DEDICATÓRIA

Ao ex-diretor do INPE, Ricardo Galvão, por seu caráter e integridade ímpares, demonstrando que, às vezes, ser exonerado é sinal de competência e honestidade. Ficará para sempre como símbolo da luta contra o obscurantismo e ignorância crescentes neste país, respaldado firme e unicamente por dados científicos.

AGRADECIMENTOS

Agradeço à Petrobras pelo apoio e liberação para o desenvolvimento deste mestrado, além do financiamento através do projeto 8310-0 FAURGS-UFRGS-PETROBRAS. Daniel Grings e a Profa. Dra. Carla Porcher são também agradecidos pela assistência com o MEV. O Prof. Dr. Silvio Buchner é reconhecido por executar análises termogravimétricas. Aos colegas do Márcio, Matheus e Larissa meu muito obrigado pela ajuda e amizade, e Roberto pela parceria e acolhida em sua nobre residência. Os técnicos e funcionários dos laboratórios do IPR-PUCRS (Victor, Victor Hugo, Nalini, Pâmela e Letícia) e UFRGS (Denise, Lucas, Gisela, Susan, Rafael, Natália, Luiz e Júlio) também são agradecidos por sua disposição e colaboração fundamental. Agradeço ainda ao Eng. Dr. Tiago Siqueira (IPR-PUCRS) por seu auxílio constante e imprescindível na execução dos experimentos hidrotermais, além da parceria e amizade. Expresso também minha gratidão ao Dr. Peter Szatmari (Petrobras) por pavimentar o caminho e indicar os rumos a serem seguidos através de décadas de pesquisa dentro da Petrobras. Cabe ainda um agradecimento especial à Monizze pelo companheirismo, carinho, incentivo e paciência ao longo destes intensos dois anos de trabalho.

Resumo: As reações de serpentinização são fundamentais para entender a atividade hidro-geotérmica em cordilheiras meso-oceânicas, ofiolitos e maciços ultramáficos, bem como a transferência de fluidos e elementos entre o manto e a crosta terrestre. Em margens divergentes, o rifteamento e extensão levam ao afinamento crustal, tornando o manto litosférico subcontinental suscetível à infiltração de água e desencadeando sua serpentinização generalizada. Neste trabalho demonstramos experimentalmente que a interação de água salina com peridotitos a 230 °C e 13,4/20,7 MPa com razão fluido/rocha constante (4:1) gera fluidos hipercalcalininos altamente redutores enriquecidos em hidrogênio, metano, cálcio e sílica em menos de 6 semanas. Os fluidos derivados da serpentinização desenvolvem pH cada vez mais elevado (até $11,3 \pm 0,1$), sustentando concentrações cada vez maiores de sílica dissolvida e, portanto, tornam-se potenciais agentes transportadores. Propomos um novo modelo de serpentinização e também que a circulação de fluidos através de falhas em escala litosférica influencia diretamente a sedimentação e diagênese em riftes. Tais fluidos de serpentinização forneciam os elementos necessários e condições de pH e oxi-redução para que carbonatos com mineralogias exóticas (\pm silicatos magnesianos \pm polimorfos de silica) possam se formar em bacias restritas, como as do pré-sal do Atlântico Sul. O transporte de sílica tem implicações para a evolução de bacias ao longo da história do planeta, desde a sedimentação química nos oceanos arqueanos à silicificação moderna nos lagos do rift africano.

Palavras-chave: Petrologia experimental; Serpentina; Pré-sal; Silicificação; Hidrotermalismo

Abstract: Serpentinization reactions are paramount to understand hydro-geothermal activity at mid-ocean ridges, ophiolites and komatiite-peridotite massifs, as well as fluid and element transfer between the Earth's mantle and crust. At divergent margins, rifting and extension lead to crustal thinning, making the shallow subcontinental lithospheric mantle susceptible to water infiltration, hence triggering widespread serpentinization. Here we experimentally demonstrate that saline water-peridotite interaction at 230°C and 13.4/20.7 MPa under constant water/rock ratio (4:1) generates highly reducing, hyperalkaline fluids enriched in hydrogen, methane, calcium and silica in under 6 weeks. Serpentinization-derived fluids develop increasingly higher pH (up to 11.3 ± 0.1), sustaining larger concentrations of dissolved silica and, thus, become suitable transport agents. We propose a new serpentinization model and that fault-controlled lithospheric-scale fluid circulation directly influences rift sedimentation and diagenesis, providing necessary elements, pH and redox conditions for exotic carbonate \pm Mg-silicate \pm silica polymorphs mineral assemblages to form in restricted basins, such as those of South Atlantic pre-salt. Silica transport has implications for the evolution of basins throughout the planet's history, from chemical sedimentation in Archean oceans to modern silicification in African rift valley lakes.

Key-words: Experimental petrology; Serpentine; Pre-salt; Silicification; Hydrothermalism

LISTA DE FIGURAS

Figura 1. Análises de XRD rocha-total do xenólito do manto PM23 (Protolith) e produtos experimentais. **a**, Os picos característicos da lizardita (12,2 e 24,5 °) aumentam de intensidade com o tempo de reação, enquanto nenhum pico de brucita ou magnetita é observado. Simultaneamente, os picos de olivina e enstatita diminuem com o tempo (e.g. 62,7 e 14 °, respectivamente). **b**, Zoom do intervalo de 9 a 17 graus da série de baixa pressão, exibindo a diminuição progressiva da intensidade no pico de enstatita com aumento concomitante no pico de lizardita. Abreviações: Cpx = clinopiroxênio (diopsídio); En = enstatita; Lz = lizardita; Ol = olivina.....pág. 28

Figura 2. Imagens eletrônicas secundárias do SEM das frações não tratada, precipitada e sobrenadante obtidas após banho ultrassônico de pó do Exp.D em álcool absoluto por 10 minutos. **a**, Amostra não tratada mostrando um grande grão de olivina revestido por serpentina de morfologia placóide. **b**, Fração precipitada coletada após banho ultrassônico com grãos parcialmente expostos de olivina (olv) e ortopiroxênio (opx) cobertos por serpentinas derivadas. O grão opx apresenta várias lamelas de exsolução de clinopiroxênio (cpx) que não são afetadas pela serpentinização. As análises de EDS confirmam que a serpentina derivada do ortopiroxênio (serp-opx, ponto 12) está depletada em sílica e alumínio relativamente à enstatita (ponto 11). **c**, Visão geral da fração sobrenadante exibindo vários grãos de serpentina placóide (platy-serp) e raros agregados de serpentina poliédrica esférica (P-serp) engolfada por proto-serpentina (Proto-serp). **d**, Área ampliada marcada pelo retângulo vermelho em "c". Agregado exibindo esferas de serpentina poliédrica de aproximadamente 1 µm de diâmetro dentro de uma matriz de proto-serpentina amorfa.pág. 29

Figura 3. Sílica rocha-total (XRF), LOI e conteúdo calculado de serpentina a partir da perda ao fogo (LOI) e TGA, considerando a lizardita como o único mineral hidratado e água estequiométrica ideal (13 wt%). Como filossilicato, a serpentina é o mineral mais propenso a ser perdido durante a preparação da amostra pós-experimento e, portanto, essas são consideradas estimativas mínimas. O ajuste (*fit*) de nossos dados (linha azul para LOI, linha verde-oliva para Serp. LOI, linha tracejada verde para Serp. TGA e linha magenta para SiO₂) demonstra que o progresso da serpentinização/hidratação

e a depleção de SiO₂ são lineares.....pág. 30

Figura 4. A primeira derivada de análises termogravimétricas do xenólito do manto PM23 (Protolith) e produtos experimentais. A temperatura de desidratação da serpentina aumenta com o tempo de reação em ambas as séries experimentais, exceto nos experimentos de duas semanas (Exp.B e B2) que mostram temperaturas mais baixas. Um pico secundário de temperatura ligeiramente mais baixa (~ 540 ° C) dentro da faixa de desidratação da serpentina é observado apenas nos Exp.C e Exp.D, sugerindo a presença de serpentina pouco cristalina. Exp.C2R é a réplica de Exp.C2.pág. 31

Figura 5. a-d, Mapas de razão atômica (EMP) de peridotito serpentinizado após 40 dias a 13,4 MPa (Exp.D). **e-g,** Evolução química das serpentinas a 13,4 MPa (n = 114). Triângulos e quadrados são plotados no eixo esquerdo; barras são plotadas no eixo direito (considerando 7, 6 e 4 Oxigênios para serpentina, piroxênio e olivina, respectivamente). Os valores do tempo zero correspondem aos minerais primários e, onde não são visíveis, as barras de erros (desvio padrão) são menores que os símbolos. Curvas são ajustes (*fits*) exponenciais dos dados. **a,** Imagem eletrônica retroespelhada de grãos de olivina e enstatita parcialmente serpentinizados. **b,** Mapa Ni/Cr exibindo distribuição homogênea entre minerais parentais e serpentinas derivadas. **c,** Mapa de Mg/Si mostrando que serpentinas derivadas de ortopiroxênio e olivina tem razões mais altas e mais baixas que os minerais parentais, respectivamente. A serp-opx tem uma média de 37,84 wt% SiO₂, indicando que a enstatita perdeu 30-35% de sua sílica (Tabelas 1-2). **d,** Mapa Al/Si evidenciando que serpentinas derivadas de ortopiroxênio e olivina têm razões mais baixas e mais altas em relação aos minerais originais, respectivamente. A serp-opx tem uma média de 1,62 wt% Al₂O₃, demonstrando que a enstatita perdeu 49-59% de seu alumínio. Embora a olivina seja desprovida de Al, o serp-olv possui uma média de 1,18 wt% Al₂O₃ (Tabelas 1-2). **e,** Razões Mg/Si e Si apfu inicialmente diferentes de ambas as serpentinas convergem exponencialmente após 40 dias, com silício abaixo da estequiometria ideal (<2 apfu). **f,** Razões Al/Si e Al apfu inicialmente diferentes de ambas as serpentinas convergem exponencialmente após 40 dias. **g,** Soma inicialmente diferente de cátions totais e octaédricos (Cations^{VI}) e Mg apfu de ambas

as serpentinas convergem exponencialmente após 40 dias; Observar quebra de escala. pág. 33

Figura 6. a-d, Mapas de razão atômica (EMP) de peridotito serpentinizado após 40 dias a 20,7 MPa (Exp.D2). e-g, Evolução química das serpentinas a 20,7 MPa (n = 184). Triângulos e quadrados são plotados no eixo esquerdo; barras são plotadas no eixo direito (considerando 7, 6 e 4 Oxigênios para serpentina, piroxênio e olivina, respectivamente). Os valores no tempo zero correspondem aos minerais originais e, onde não são visíveis, as barras de erros (desvios padrão) são menores que os símbolos. Curvas são ajustes exponenciais dos dados. **a**, Imagem eletrônica retroespelhada de grãos de olivina e enstatita parcialmente serpentinizados. **b**, Mapa Ni/Cr exibindo distribuição homogênea entre minerais parentais e serpentinas derivadas. **c**, Mapa de Mg/Si mostrando que as serpentinas derivadas de ortopiroxênio e olivina tem razões mais altas e mais baixas que os minerais parentais, respectivamente. A serp-opx tem uma média de 41,76 wt% SiO₂, indicando que a enstatita perdeu 23-28% de sua sílica (Tabelas 1-2). **d**, Mapa Al/Si evidenciando que as serpentinas derivadas de ortopiroxênio e olivina têm razões mais baixas e mais altas em relação aos minerais originais, respectivamente. A serp-opx tem em média 1,78 wt% Al₂O₃, demonstrando que a enstatita perdeu 41-57% de seu alumínio. Embora a olivina seja desprovida de Al, o serp-olv possui uma média de 1,24 wt% de Al₂O₃ (Tabelas 1-2). **e**, Razões Mg/Si e Si apfu inicialmente diferentes de ambas as serpentinas convergem exponencialmente após 40 dias, com o silício se aproximando da estequiometria ideal (2 apfu). **f**, Razões Al/Si e Al apfu inicialmente diferentes de ambas as serpentinas convergem exponencialmente após 40 dias. **g**, Soma inicialmente diferente de cátions totais e octaédricos (Cations^{VI}) e Mg apfu de ambas as serpentinas convergem exponencialmente após 40 dias; Observar quebra de escala. pág. 34

Figura 7. Imagens de elétrons retroespelhados de grãos de diopsídio (cpx) com raras feições de dissolução. **a**, Grão de clinopiroxeno parcialmente dissolvido após ca. 20 dias a 13,4 MPa (Exp.C). A área cinza mais escura no canto superior direito do grão é uma porção do mesmo mineral que não foi exposta pelo polimento. **b**, Grão diopsídio exibindo bordas dissolvidas após apenas 5 dias a 20,7 MPa (Exp.A2). pág. 35

Figura 8. Imagens de elétrons retroespalhados de enstatita (opx) parcialmente serpentinizada com lamelas submicrométricas de exsolução de diopsídio (cpx) (cor cinza clara/esbranquiçada) não afetadas por lizardita recém-formada (serp-opx) em fraturas e ao redor do ortopiroxênio. **a**, Múltiplas lamelas de exsolução de cpx formam cúspides resistentes atravessando serpentina recém formada em uma fratura que divide um cristal maior de opx (Exp.C). **b**, Lamelas esbranquiçadas de cpx não afetadas por serp-opx que envolve opx (Exp.D) **c**, Lamelas de exsolução de diopsídio (cinza clara) não afetadas por serpentinas formadas ao redor e dentro de fraturas na enstatita. A serpentização segue fraturas e planos cristalográficos do ortopiroxênio (Exp.D). pág. 36

Figura 9. Imagem de elétron retroespalhado (BSE) e mapas elementares quantitativos (da EMP) de um cristal de espinélio extensivamente dissolvido (Spl) do Exp.D2. **a**, Imagem BSE de um grão de espinélio apresentando uma ampla borda de dissolução. Olivina (olv), enstatita (opx) e serpentina derivada (Serp-opx) também são visíveis no quadro. **b**, Mapa de Al_2O_3 exibindo que a borda de dissolução do espinélio possui 27,7 a 34,7 wt% de óxido de alumínio, o que equivale a uma perda de 30 a 45% do seu conteúdo inicial de alumínio (Tabela 1). Serpentina derivada de olivina (serp-olv) e serp-opx também são destacadas. **c**, Mapa de Cr_2O_3 mostrando que o cromo está concentrado na borda em relação ao núcleo. **d**, Mapa de MgO evidenciando que a concentração de magnésio é ligeiramente maior nas partes externas das bordas dissolvidas e do cristal relíquiar. **e**, Mapa de FeO (ferro total) ilustrando que o ferro está concentrado na borda em relação ao núcleo. **f**, Mapa de MnO exibindo que o manganês está altamente concentrado na borda em relação ao núcleo, atingindo aproximadamente 4 wt%. **g**, Mapa de TiO_2 mostrando que o titânio é concentrado na borda em relação ao núcleo. Pontos de alta concentração dentro da borda dissolvida possivelmente correspondem a locais de nucleação. **h**, Mapa da soma total de óxidos. pág. 37

Figura 10. Aumento do volume da rocha em função da percentagem em peso de serpentina para os dois conjuntos de pressão. Os volumes iniciais foram calculados assumindo densidade média dos peridotitos ($3,2873 \text{ g/cm}^3$), enquanto os volumes de produtos serpentinizados foram calculados aplicando a fórmula empírica da densidade-grau de serpentização ($p = -0,761x + 3,2873$) de Pinto *et al.*, (2017) (e referências citadas), onde "x" representa a serpentina modal estimada pela perda ao

fogo (LOI). Nossos dados resultam numa correlação linear positiva entre o aumento do volume da rocha e a serpentinização. Além disso, experimentos de baixa e alta pressão (A e B2), ambos contendo 3,31% em peso de serpentina, resultaram em um aumento de volume quase idêntico de +1,47 e +1,50%, respectivamente, demonstrando expansão de volume independentemente da pressão e excelente concordância dos dados. Além disso, considerando que os peridotitos completamente serpentinizados contêm em média 90 wt% de serpentina, 7 wt% de magnetita e 3 wt% de brucita, nossos resultados sugerem um aumento de volume da rocha superior a 31,5% ao término da reação, em consonância com estimativas anteriores..... pág. 39

Figura 11. Concentração de Si aquosa medida e calculada e evolução do pH ao longo dos experimentos. A concentração esperada de silício aquoso foi calculada subtraindo a massa de água medida nos produtos da reação (LOI) da massa inicial da solução de entrada, em conjunto com balanço de massa do SiO_2 de rocha-total (XRF) pré e pós-experimento. O pH medido ($25\text{ }^{\circ}\text{C}$) aumenta exponencialmente e, após 20 dias, tende a estabilizar em torno de 11,3 e 10,7 para a série de baixa e alta pressão, respectivamente. Nossas estimativas sugerem que, a $20,7\text{ MPa}$, os fluidos de serpentinização ficam supersaturados em Si em menos de 40 dias e, após o resfriamento até a temperatura ambiente, a sílica aquosa é nucleada (setas pretas) como nanopartículas de sílica. Portanto, esse comportamento resulta em concentrações medidas de $\text{Si}_{(\text{aq})}$ progressivamente mais baixas conforme os fluidos se tornam mais saturados. As barras de erro são desvios padrão de análises duplicadas e, onde não visíveis, são menores que os símbolos. A concentração de Si da solução inicial é igual para ambos conjuntos. Valores da solubilidade da sílica a partir de dados experimentais (Gunnarsson & Arnórsson, 2000). pág. 40

Figura 12. Modelo esquemático da serpentinização de peridotitos em dois estágios. Nossos dados são representados por linhas cheias, enquanto linhas tracejadas são extrapolações baseadas na literatura. A primeira etapa foi abordada por nossos experimentos e anteriores (Huang *et al.*, 2017), caracterizando-se pela geração simultânea de serpentina rica em Al a partir do ortopiroxênio e da olivina. O pH do fluido aumenta e estabiliza (> 10), permitindo que o excesso de $\text{SiO}_{2(\text{aq})}$ ascenda por sistemas de circulação abertos, enquanto o clinopiroxênio e o espinélio são totalmente

dissolvidos. Somente traços de brucita e magnetita podem se formar devido às atividades elevadas de alumínio e sílica ($a\text{SiO}_2$), com a produção de H_2 catalisada por espinélio ligada à incorporação de Fe^{3+} pela serpentina. A segunda fase é caracterizada pela hidratação da olivina, resultando em serpentina rica em Mg ± brucita (Frost & Beard, 2007; Andreani *et al.*, 2013; McCollom *et al.*, 2016). Esse estágio possui $a\text{SiO}_2$ notavelmente baixa, favorecendo a estabilidade da brucita e a decomposição do componente de ferro da serpentina em magnetita + sílica + água + H_2 (Frost & Beard, 2007; Katayama *et al.*, 2010). Além de promover o empobrecimento de sílica e H_2 controlado por magnetita, a desestabilização da serpentina pode precipitar ligas de Ni-Fe (Frost & Beard, 2007), provavelmente associadas à serp-olv rica em Ni. Além disso, as texturas mais tardias dos serpentinitos compreendem a substituição exclusiva da olivina reliquiar (Andreani *et al.*, 2013) por veios ricos em magnetita e pobres em serpentina associados a ligas de Ni-Fe (Katayama *et al.*, 2010). Além disso, sob condições adequadas de PT, essas ligas podem catalisar a hidrogenação do CO_2 (Etiope & Sherwood Lollar, 2013), potencializando a metanogênese. Como os peridotitos contêm no máximo 60% de piroxênio modal, o estágio 1 (pobre em magnetita) se encaixa em até 60-75% de progresso da reação (Oufi *et al.*, 2002; Bach *et al.*, 2006; Andreani *et al.*, 2013), após o qual a serpentinização tardia exclusivamente da olivina produz magnetita exponencialmente (Toft *et al.*, 1990; Oufi *et al.*, 2002; Bach *et al.*, 2006; Seyfried *et al.*, 2007; Andreani *et al.*, 2013). A duração de cada estágio depende da composição modal do peridotito, o que implica que os litotipos mais ricos em olivina têm segundos estágios cada vez mais longos e taxas mais lentas. Brc = brucita; Mag = magnetita; Sp = espinélio.

..... pág. 44

Figura 13. Modelo esquemático da influência de fluidos derivados de serpentinização na província do pré-sal do Atlântico Sul (fora de escala). **a**, A percolação de água controlada por falhas (setas azuis) após vulcanismo expressivo desencadeia a serpentinização de peridotitos residuais no manto. As câmaras magmáticas na base da crosta continental hiperextendida (<5-10 km de espessura, cf. (Zalán *et al.*, 2011) fornecem continuamente CO_2 (setas pretas) à bacia através de falhas/fraturas, facilitando a deposição de carbonatos. **b**, Os fluidos hiperálcalinos derivados da serpentinização enriquecidos em sílica, cálcio, metano e hidrogênio, geram plumas hidrotermais de temperatura moderada-alta (200-300 °C) (setas laranja). Dependendo da eficiência da circulação de água, essas frentes de serpentinização podem induzir

uma anomalia térmica de 20-30 mW/m² em 2-6 Ma após o início da serpentinização (Delescluse & Chamot-rooke, 2008), aumentando o gradiente geotérmico local. Ao atingir águas superficiais mais frias e/ou reservatórios carbonáticos ± saturados em HC, a exalação hidrotermal nuclearia grandes quantidades de sílica e, se as águas locais homogeneizadas alcançassem pH> 10, esferulitos e argilas magnesianas poderiam precipitar. A neutralização de fluidos hiperalcalinos ricos em sílica pela mistura em várias proporções com fluidos ácidos (magmáticos-hidrotermais ± CO₂ e/ou meteóricos) levaria à nucleação quase instantânea (Tobler *et al.*, 2009) ao longo de condutos/planos de falhas, explicando a silicificação generalizada em falhas de descolamento (Bonnemains *et al.*, 2017). Da mesma forma, a neutralização do pH por águas meteóricas durante crises de alcalinidade de episódios úmidos (Wright & Barnett, 2015; Tritlla *et al.*, 2018) ilustra ainda um controle deposicional climático adicional. As frequentes inclusões flúidas de CO₂-HC em cimentos silicosos hidrotermais (Poros *et al.*, 2017; Girard & Miguel, 2018) e a sincronicidade com a migração de HC (Tritlla *et al.*, 2018) também sugerem que os fluidos de serpentinização e o fluxo térmico associado podem ter influenciado localmente a síntese/degradação de HC líquidos. pág. 46

LISTA DE TABELAS

- Tabela 1-** EMPA de minerais primários e Compilação de dados de rocha.... (Anexo A)
Tabela 2- EMPA de serpentinas(Anexo B)
Tabela 3- Análises de XRF rocha-total.....(Anexo C)
Tabela 4- Análises dos fluidos-gases de serpentinização(Anexo D)

SUMÁRIO

	pág
RESUMO.....	1
ABSTRACT	2
ESTRUTURA DA DISSERTAÇÃO.....	11
CAPÍTULO I – TEXTO INTEGRADOR.....	12
a) Introdução.....	12
b) Objetivos.....	13
c) O estado da arte da serpentinização experimental.....	13
d) Materiais e métodos.....	14
e) Contexto geológico da província pré-sal do Atlântico Sul.....	17
f) Resumo dos principais resultados e interpretações.....	18
g) Conclusões.....	19
h) Referências bibliográficas.....	20
CAPÍTULO II – ARTIGO CIENTÍFICO INTERNACIONAL	26
a) Introduction.....	26
b) Results.....	27
i. Serpentinization of olivine and orthopyroxene.....	27
ii. Dissolution of clinopyroxene and spinel.....	35
iii. Whole-rock geochemistry, mass-volume increase and serpentinization-derived fluids.....	38
c) Discussions and Conclusion.....	41
i. Understanding serpentinization in two steps.....	41
ii. A mantle influenced petroleum system: The South Atlantic pre-salt.....	45
d) Methods.....	47
e) References.....	53
CAPÍTULO III – COMPLEMENTOS	59
• ANEXO A (Tabela 1) – Table 1	
• ANEXO B (Tabela 2) – Table 2	
• ANEXO C (Tabela 3) – Table 3	
• ANEXO D (Tabela 4) – Table 4	
• ANEXO E (Resumo publicado em congresso internacional)	
• ANEXO F (Artigo internacional publicado – Portella <i>et al.</i> (2019) - Minerals)	

ESTRUTURA DA DISSERTAÇÃO

Esta dissertação de mestrado está estruturada em um artigo submetido em periódico classificado no estrato Qualis-CAPES (A1). A sua organização compreende as seguintes partes principais:

TEXTO INTEGRADOR:

Texto Integrador composto pelos seguintes capítulos: a) introdução com a formulação do problema de investigação e a hipótese; b) objetivos da pesquisa; c) o estado da arte do tema da pesquisa; d) os materiais e métodos utilizados; e) o contexto geológico da área (se houver) ou do objeto de estudo; f) resumo dos principais resultados obtidos, interpretações desenvolvidas nos artigos e discussão integradora dos resultados; g) conclusões; h) referências bibliográficas.

ARTIGOS:

Corpo Principal da Dissertação, constituído do artigo “**The link between serpentinization, silica transport, carbonates and rift sedimentation**” conforme os itens 1.1; 1.2 e/ou 1.3 da norma 118.

COMPLEMENTOS (Opcional):

Anexos, compreendendo: tabelas, cálculos, gráficos (figuras, diagramas, mapas, seções) e fotografias, os quais devem ser referidos no Texto Integrador, identificados por letras maiúsculas, consecutivas, e pelos respectivos títulos. Também poderão ser inseridos nos Anexos resumos, artigos publicados em eventos e outros artigos em que o mestrando seja primeiro autor ou coautor, produzidos durante o Curso de Mestrado.

CAPÍTULO I – TEXTO INTEGRADOR

a) Introdução

Desde a descoberta de campos gigantes de petróleo hospedados em carbonatos na província pré-sal offshore brasileira, sua evolução geológica tem sido intensamente discutida. Os reservatórios do pré-sal são caracterizados por uma paragênese incomum, composta por carbonatos \pm esmectitas magnesianas \pm polimorfos de sílica (Wright & Barnett, 2015; Saller *et al.*, 2016; Tutolo & Tosca, 2018).

Embora onipresentes, a origem do Si e do Mg nessas rochas não é clara. Alguns autores evocam intemperismo e lixiviação dos basaltos Paraná-Etendeka por drenagens vulcânicas (Wright, 2012; Szatmari & Milani, 2016) e/ou alteração do embasamento vulcânico subjacente (Szatmari & Milani, 2016; Rogerson *et al.*, 2017; Teboul *et al.*, 2017, 2019). Alternativamente, foi proposto que a serpentinização do manto exumado pode influenciar significativamente a dolomitização e a silicificação em bacias restritas (Pinto *et al.*, 2017). No entanto, faltam dados experimentais que corroborem a depleção de sílica durante a serpentinização e a capacidade de transporte dos fluidos derivados.

Apresentamos aqui dois conjuntos de experimentos de serpentinização que contemplam a evolução química dos fluidos e minerais durante interações entre água salina e peridotitos ($230\text{ }^{\circ}\text{C}$) com razão fluido/rocha constante ($F/R = 4:1$) sob 13,4 e 20,7 MPa. Tais condições simulam realisticamente a hidratação do manto depletado subjacente à província pré-sal, que provavelmente estava se desenvolvendo prévia e simultaneamente à deposição dos reservatórios carbonáticos. Os fluidos derivados da serpentinização poderiam, portanto, migrar através de falhas e influenciar a sedimentação e diagênese no pré-sal.

b) Objetivos

Este trabalho tem como objetivo propor novos modelos/soluções para duas questões de longa data: (1) como as reações de serpentinização se desenvolvem e quais elementos são transferidos das rochas para os fluidos; (2) qual é a fonte do Si e Mg responsável pela paragênese de minerais exóticos (carbonatos ± esmectitas magnesiana ± polimorfos de sílica) observada em reservatórios carbonáticos de petróleo da província cretássica pré-sal do Atlântico Sul.

c) O estado da arte da serpentinização experimental

As reações de serpentinização, i.e. de hidratação das olivinas e piroxênios presentes em rochas maficas-ultramáficas, são observadas em diversos ambientes, desde complexos ofiolíticos e intrusões ígneas a cinturões metamórficos de baixo grau. As serpentinas podem conter até 13 wt% de H₂O e, por isso, tem função importante no ciclo global da água em zonas de subducção (Müntner *et al.*, 2010). Apesar disso, estudos dos fluidos resultantes do processo de serpentinização não foram abundantes até 20 anos atrás.

Paradoxalmente, a síntese de CH₄ e H₂ através da serpentinização de rochas ultramáficas foi identificada e documentada a mais de 50 anos (Thayer, 1966). Recentemente tais reações ganharam interesse renovado devido às suas implicações para a origem da vida (Russell *et al.*, 2010), a possível influência na composição da atmosfera de Marte e outros planetas (Tobie *et al.*, 2006; Atreya *et al.*, 2007; Etiope *et al.*, 2013) e como possível fonte subordinada de metano em reservatórios de afinidade ígnea (Szatmari, 1989; Sherwood Lollar *et al.*, 2002; Szatmari *et al.*, 2011; Etiope & Schoell, 2014).

Contudo, estudos experimentais focados na geração de sílica aquosa por meio de reações de serpentinização de rochas maficas-ultramáficas ainda não foram publicados. (Seyfried *et al.*, 2007) realizaram experimentos envolvendo água do mar e Iherzolitos a 200 °C e 500 bar na tentativa de simular os fluidos hiperalcalinos do campo hidrotermal de Lost City. Tais autores reportam que a serpentina é o principal mineral secundário e que apenas traços de magnetita foram observados, o que implica que a geração de H₂ é acomodada pela incorporação de Fe³⁺ pela serpentina. Outrossim, sugerem ainda que o clinopiroxênio é parcialmente dissolvido e reportam 0-430 µmol/kg Si_(aq) nos fluidos derivados. Similarmente, (Marcaillou *et al.*, 2011)

também serpentinizaram Iherzolito em pó em água pura a 300 °C/300 bar, e concluíram que a razão $\text{Fe}^{3+}/\text{Fe}_{\text{total}}$ é linearmente dependente da produção de hidrogênio. O mesmo estudo revela que a serpentina pode conter 0 a 100% de ferro férrico, incluindo até 12% de ferro tetraédrico, enquanto o $\text{Si}_{(\text{aq})}$ variou de 36-262 $\mu\text{mol/kg}$. Nos experimentos de (McCollom *et al.*, 2016), olivinas pulverizadas num intervalo de 200-320 °C a 35 MPa foram hidratadas visando entender a produção de H_2 , sendo observada a liberação de 20-80 $\mu\text{mol/kg}$ $\text{Si}_{(\text{aq})}$ ao longo de semanas até quase 1 ano. Mais recentemente, (Huang *et al.*, 2017), demonstraram que a taxa de serpentinização de peridotitos é fortemente influenciada pelo tamanho dos grãos dos reagentes, com tamanhos menores resultando em taxas mais rápidas. Estes autores mostram ainda que a serpentinização de peridotitos é acelerada pelo Al e Cr liberados por piroxênios e espinélios, resultando em taxas ~5x mais rápidas em comparação com a hidratação da olivina sozinha.

d) Materiais e métodos

O material reagente foi preparado a partir do xenólito mantélico PM23, um peridotito fanerítico composto de olivina, enstatita, diopsídio, espinélio, carbonatos intersticiais e traços de anfibólio. O peridotito foi amostrado no campo vulcânico Gobernador Gregores (Argentina), onde ocorre como xenólitos subesféricos (até 60 cm de diâmetro) envoltos por basaltos alcalinos. Convergindo fluorescência de raios-X (XRF) de rocha-total e análises de microssonda eletrônica (EMPA) em minerais primários, a composição modal do material inicial foi determinada como 76% de olivina, 16% de enstatita, 6% de diopsídio e 2% de espinélio, portanto caracterizada como um Iherzolito-harzburgito (Tabela 1). Para avaliar a representatividade do material inicial em relação ao manto depletado, combinamos dados de EMPA e modas minerais de compilações de peridotitos abissais residuais (Warren, 2016) e serpentinitos (Deschamps *et al.*, 2013; Peters *et al.*, 2017) da literatura para estimar as composições médias de rocha-total de vários litotipos (Tabela 1). A amostra PM23 apresenta mineralogia modal e geoquímica de rocha-total semelhante aos peridotitos residuais médios e, portanto, pode ser considerada um bom análogo do manto superior depletado (Tabela 1).

Para evitar a contaminação por sílica durante a preparação, recipientes/utensílios de cerâmica e plástico foram utilizados sempre que possível. A amostra foi desagregada usando um moinho de placas de cerâmica, moída manualmente com

pistilo e gral de cerâmica e, em seguida, peneirada a seco até a fração 63-180 µm, dentro da faixa típica de *gouges* de falhas (Wang *et al.*, 2016). Lixiviação ácida usando HCl 0,1 M durante banho ultrassônico foi aplicada à amostra para remover carbonatos intersticiais supergênicos e partículas muito finas. Posteriormente, o pó foi lavado várias vezes, peneirado por via úmida com água deionizada abundante e seco a 50 °C por 24h. A perda ao fogo (LOI) do pó de peridotito inicial foi inferior a 0,001 wt% (Tabela 1), confirmando que a amostra é fresca e que todos os carbonatos foram removidos com sucesso pelo ataque ácido. Observações do pó inicial por microscopia eletrônica de varredura (SEM) indicam que o tamanho médio das partículas está mais próximo do limite superior (180 µm), com alguns grãos chegando a 300 µm, provavelmente devido ao hábito prismático dos piroxênios, que podem ser peneirados ao longo de seu eixo longo.

A perda ao fogo, elementos maiores e menores do peridotito inicial foram determinados por XRF, enquanto os minerais primários foram identificados por difração de raios-X (XRD) e sua composição resolvida por EMPA em lâminas delgadas (Tabela 1). Mais de 30 análises foram realizadas para cada silicato e cerca de 11 análises para espinélio, todas com elementos maiores com erro relativo abaixo de 3%, o que sugere que os minerais primários são homogêneos. Um fluido de salinidade da água do mar (33 g / L = 0,56 M NaCl) foi preparado através da adição de cloreto de sódio de grau analítico à água deionizada. A solução foi totalmente equilibrada com dióxido de carbono atmosférico em condições ambientais e, considerando uma concentração média de CO₂ (atm) de 390 ppm, sua concentração dissolvida foi estimada em $7,96 \times 10^{-3}$ mmol/kg usando o software PHREEQC-v3 (Parkhurst and Appelo, 2013).

Configuração experimental

Dois conjuntos de experimentos com pressão “baixa” (13,4 MPa, série Exp.A-D) e “alta” (20,7 MPa, série Exp.A2-D2) e temperatura constante (230 °C) foram projetados para investigar os efeitos de sobrecarga na cinética da serpentinização. Todos os experimentos foram realizados no Instituto de Petróleo e Recursos Naturais (IPR-PUCRS) em um reator de Hastelloy™ de alta pressão (sem agitação) de 75 mL de capacidade da *Parr Instrument Company*, equipado com um manômetro e um controlador automático de temperatura conectado a uma mufla de aquecimento. O pó de peridotito (14 g) e a solução salina artificial (56 g) foram adicionados para atingir a

razão de massa inicial ($F/R = 4: 1$), que simula a faixa inferior da serpentinização de harzburgitos na cordilheira meso-atlântica (Vils *et al.*, 2009). Apenas o Exp.B foi realizado com 8 g de peridotito e 32 g de solução salina, contudo, mantendo a mesma relação F/R . A mistura foi agitada e subsequentemente seu $pH_{25\text{ }^{\circ}\text{C}}$ foi medido usando um eletrodo 913 Metrohm Pt1000 com uma incerteza de aproximadamente $\pm 0,1$ unidades do valor reportado. O ar no reator foi purgado duas vezes com gás argônio pressurizado até 200 bar e drenado sucessivamente até 30 bar, antes que o espaço residual (ca. 15 cm³) fosse finalmente preenchido argônio puro, garantindo uma atmosfera de reação inerte. O reator foi aquecido a taxa constante até 230 °C e deixado reagir sob pressões saturadas de vapor de $13,4 \pm 0,8$ ou $20,7 \pm 0,8$ MPa (séries "baixa" e "alta", respectivamente) em experimentos individuais por aproximadamente 5, 14, 20 e 40 dias. O início dos experimentos foi considerado somente após a temperatura alvo ser atingida. Durante as corridas a temperatura variou $\pm 5\text{ }^{\circ}\text{C}$ principalmente devido à oscilação da temperatura ambiente. Para evitar alterações na razão F/R , todas as amostras foram coletadas em condições ambiente após o término dos experimentos. Foi feita uma réplica (Exp.C2R) do experimento (Exp.C2) para garantir a reproduzibilidade dos resultados.

Procedimento pós-experimento

No final de cada experimento, o aquecimento foi desligado e o reator resfriou naturalmente até a temperatura ambiente enquanto ainda pressurizado com o gás argônio inicial. A têmpera não foi aplicada para evitar a precipitação induzida de sílica durante o resfriamento abrupto. As amostras de gás foram coletadas (somente na série de alta pressão) do reator pressurizado usando um dispositivo de amostragem de pressão constante (1 bar) acoplado à válvula do reator. As amostras foram imediatamente analisadas por cromatografia gasosa (GC) usando um detector de condutividade térmica (TCD) para H₂ e CO₂ e um detector de ionização de chama (FID) para o conteúdo de HC. Em todos os experimentos o reator foi cuidadosamente despressurizado até 1 atm usando a válvula bidirecional antes de ser aberto, e o pH 25 °C foi imediatamente medido dentro do copo do reator.

As amostras de fluido foram recuperadas, pesadas e centrifugadas a 4000 rpm por 5 min antes que o $pH_{25\text{ }^{\circ}\text{C}}$ fosse medido novamente. As medições no fluido centrifugado e não centrifugado sempre apresentaram valores coerentes de pH dentro da incerteza analítica. Foram retiradas duas alíquotas de 5 g do fluido centrifugado de cada

experimento, uma das quais foi ligeiramente acidificada com 5% de HNO₃ e a outra foi mantida sem tratamento. Essas alíquotas foram diluídas 10x com água deionizada antes das análises químicas usando espectroscopia de emissão óptica de plasma acoplada indutivamente (ICP-OES).

Os produtos sólidos foram lavados com água deionizada e centrifugados sucessivamente três vezes a 4000 rpm por 5 min para eliminar todo o resíduo salino e, em seguida, secos em uma placa de Petri por 36-72 h a 40 °C. Os sólidos secos recuperados sempre variaram menos de +1 wt% em comparação com a massa inicial de reagente, garantindo a representatividade da amostra. O pó foi homogeneizado usando pistilo e gral de cerâmica, com subamostras coletadas para XRF e XRD rocha-total, espectroscopia dispersiva de energia acoplada SEM (EDS), análise termogravimétrica (TGA) e caracterização por EMP. Seções polidas impregnadas com resina foram usadas para obter imagens com SEM, bem como para análises quantitativas de minerais primários e secundários por EMP.

e) Contexto geológico da província pré-sal do Atlântico Sul

As espessas sucessões eocretássicas pré-sal foram depositadas nas margens continentais da América do Sul e da África durante rifteamento e extensão, que culminaram com a abertura do Atlântico Sul. O stress distribuído gerou vulcanismo anômalo em ambas as margens conjugadas em zonas de extensão litosférica intracontinental ativa (Foulger, 2018). A deposição dos carbonatos foi interdigitada com múltiplos fluxos de lava (Alves *et al.*, 2019) e intrudida por soleiras e diques, que podem estar associados a expressivos *vents* hidrotermais (Alvarenga *et al.*, 2016). Esses reservatórios de hidrocarbonetos (HC) apresentam fases gasosas com até 80% de CO₂ mantélico e também He (Neto *et al.*, 2012), atestando intensa contribuição mantélica e rotas de migração provavelmente relacionadas a falhas de escala crustal. Tais falhas foram mapeadas até o topo do manto, onde a serpentinização ocorre com uma extensão progressivamente menor até 6-8 km de profundidade em porções exumadas (Zalán *et al.*, 2011). Esse sistema petrolífero foi subsequentemente selado por acumulações de sal em toda a bacia (localmente com >2 km de espessura) em menos de 600 ka (Dias, 2004), e modelagens termodinâmicas recentes sugerem que esse gigante de sal poderia ter sido formado por salmouras hidrotermais derivadas da serpentinização (Debure *et al.*, 2019).

As rochas reservatório do pré-sal são caracterizadas por uma assembléia mineralógica incomum, composta por carbonatos, \pm esmectitas magnesianas \pm polimorfos de sílica, com estruturas/texturas sedimentares exóticas formadas em lagos restritos de água doce a progressivamente mais salina e alcalina (Wright & Barnett, 2015; Saller *et al.*, 2016; Tutolo & Tosca, 2018). A água lacustre continha alta concentração de sílica (Wright, 2012; Wright & Barnett, 2015; Saller *et al.*, 2016) e dados experimentais sugerem que pH elevado (10-10,5) teria sido necessário para precipitar carbonatos esferulíticos e argilas magnesianas autigênicas comumente observadas nesses reservatórios (Tutolo & Tosca, 2018).

Sílica sin-sedimentar e intervalos parcial a completamente silicificados e/ou dolomitizados, associados à atividade diagenética-hidrotermal, são comuns em ambas as margens (Herlinger *et al.*, 2017; Poros *et al.*, 2017; Teboul *et al.*, 2017, 2019; Girard & Miguel, 2018; Tritlla *et al.*, 2018), com carbonatos exibindo várias gerações de cimentos (Herlinger *et al.*, 2017; Girard & Miguel, 2018; Tritlla *et al.*, 2018; Teboul *et al.*, 2019). Na Bacia de Campos (Brasil), a silicificação tardia é atribuída a uma pluma hidrotermal de alta temperatura (90-170°C) e salinidade moderada-alta concomitante à migração de HC (Tritlla *et al.*, 2018). Além disso, intenso fraturamento, dissolução e diagênese do reservatório estão ligadas à circulação focada de fluidos hidrotermais profundos (Herlinger *et al.*, 2017). Analogamente, na Bacia de Kwanza (Angola), salmouras de alta temperatura (150-200 °C) contendo CO₂ e HC controladas por falhas submeteram os reservatórios a fluxos de calor anormalmente altos (Girard & Miguel, 2018). Ainda na margem angolana, precipitados de sílica se formaram a partir de fluidos quentes (98-123 °C) contendo CO₂ e HC que migraram por falhas em combinação com *build-ups* carbonáticos (Poros *et al.*, 2017).

f) Resumo dos principais resultados e interpretações

Os principais resultados e discussões acerca das reações de serpentinização e a influência dos fluidos derivados na província pré-sal do Atlântico Sul estão sintetizados nas figuras 4 e 5 do artigo (Capítulo 2), respectivamente. De forma suscinta, a serpentinização pode ser dividida em 2 etapas, a primeira caracterizada pela hidratação simultânea da olivina e piroxênio com liberação de sílica aquosa e a segunda pela serpentinização de olivina reliquiar com formação exponencial de magnetita. Os fluidos derivados da serpentinização experimental são similares aos do campo hidrotermal de Lost City, sugerindo que o mesmo é um análogo natural dos

nossos experimentos. Nossos fluidos também se assemelham quimicamente às águas lacustres onde esferulitos e argilas magnesianas podem precipitar, sugerindo que a serpentinização possivelmente influenciou a sedimentação no pré-sal.

g) Conclusões;

A serpentinização de peridotitos é um processo complexo de hidratação que envolve múltiplas reações em duas etapas, não podendo ser completamente compreendido apenas pela hidratação da olivina. A primeira etapa (até 60-75% do progresso da reação) pode ser resumida pela geração simultânea de serpentina rica em Al a partir do ortopiroxênio e olivina, sendo acelerada pela dissolução dos espinélios. Concomitantemente, a dissolução dos clinopiroxênios libera Ca nos fluidos derivados, não sendo precursores de serpentina. A segunda fase da serpentinização (75-100%) é caracterizada pela hidratação da olivina na ausência de piroxênios e espinélios, com a formação de serpentina magnesiana, magnetita \pm brucita \pm ligas Ni-Fe.

Nossos dados indicam que a hidratação de 1 m³ de peridotito resultaria em 1,31 m³ de serpentinito (>31,5 % de aumento de volume) e cerca de 33 kg de sílica aquosa após o término da reação (<6-12 meses), demonstrando que a serpentinização não é isovolumétrica nem isoquímica, mas geologicamente instantânea. Os fluidos derivados da serpentinização de peridotitos são hiperalcalinos (pH >10) e enriquecidos em H₂, CH₄, Si e Ca, sendo, portanto, potenciais agentes de transporte do silício aquoso. Nossos fluidos experimentais se assemelham aos do campo hidrotermal de Lost City (Seyfried *et al.*, 2015), onde a serpentinização de peridotitos acontece em subsuperfície a 200 \pm 50 °C (Allen & Seyfried, 2004), sugerindo que o mesmo é um análogo natural dos nossos experimentos. Além disso, nossos fluidos são também composicionalmente compatíveis com a água que poderia ter precipitado esferulitos e argilas magnesianas nos lagos do pré-sal (Tutolo & Tosca, 2018). Portanto, sugerimos que os fluidos hidrotermais derivados da serpentinização do manto depletado sob a província pré-sal do Atlântico Sul podem ter influenciado diretamente a sedimentação e diagênese (silicificação) dos reservatórios carbonáticos.

h) Referências bibliográficas

- Allen, D. E., & W. E. Seyfried, 2004, Serpentinization and heat generation: Constraints from Lost City and Rainbow hydrothermal systems: *Geochimica et Cosmochimica Acta*, v. 68, no. 6, p. 1347–1354, doi:10.1016/j.gca.2003.09.003.
- Alvarenga, R. S., D. Iacopini, J. Kuchle, C. M. S. Scherer, and K. Goldberg, 2016, Seismic characteristics and distribution of hydrothermal vent complexes in the Cretaceous offshore rift section of the Campos Basin, offshore Brazil: *Marine and Petroleum Geology*, v. 74, p. 12–25, doi:10.1016/j.marpetgeo.2016.03.030.
- Alves, S., G. Medeiros, J. Teixeira, A. Fernando, M. Freire, E. Fernandes, and D. Lima, 2019, Characterization of subaerial volcanic facies using acoustic image logs : Lithofacies and log-facies of a lava-flow deposit in the Brazilian pre-salt , deepwater of Santos Basin: *Marine and Petroleum Geology*, v. 99, no. September 2018, p. 156–174, doi:10.1016/j.marpetgeo.2018.09.029.
- Andreani, M., M. Muñoz, C. Marcaillou, and A. Delacour, 2013, μ XANES study of iron redox state in serpentine during oceanic serpentinization: *Lithos*, v. 178, p. 70–83, doi:10.1016/j.lithos.2013.04.008.
- Atreya, S. K., P. R. Mahaffy, and A.-S. Wong, 2007, Methane and related trace species on Mars: Origin, loss, implications for life, and habitability.: *Planetary and Space Science*, v. 55, p. 358–369.
- Bach, W., H. Paulick, C. J. Garrido, B. Ildefonse, W. P. Meurer, and S. E. Humphris, 2006, Unraveling the sequence of serpentinization reactions: Petrography, mineral chemistry, and petrophysics of serpentinites from MAR 15°N (ODP Leg 209, Site 1274): *Geophysical Research Letters*, v. 33, no. 13, doi:10.1029/2006GL025681.
- Bonnemains, D., J. Escartín, C. Mével, M. Andreani, and A. Verlaguet, 2017, Pervasive silicification and hanging wall overplating along the 13°20'N oceanic detachment fault (Mid-Atlantic Ridge): *Geochemistry, Geophysics, Geosystems*, v. 18, no. 6, p. 2028–2053, doi:10.1002/2017GC006846.
- Debure, M., A. Lassin, N. C. Marty, F. Claret, A. Virgone, S. Calassou, and E. C. Gaucher, 2019, Thermodynamic evidence of giant salt deposit formation by serpentinization: an alternative mechanism to solar evaporation: *Scientific Reports*, v. 9, no. 1, p. 1–11, doi:10.1038/s41598-019-48138-9.
- Delescluse, M., & N. Chamot-rooke, 2008, Serpentinization pulse in the actively deforming Central Indian Basin: *Earth and Planetary Science Letters*, v. 276, no.

- 1–2, p. 140–151, doi:10.1016/j.epsl.2008.09.017.
- Deschamps, F., M. Godard, S. Guillot, and K. Hattori, 2013, Geochemistry of subduction zone serpentinites: A review: *Lithos*, v. 178, p. 96–127, doi:10.1016/j.lithos.2013.05.019.
- Dias, J. L., 2004, Tectônica, estratigrafia e sedimentação no Andar Aptiano da margem leste brasileira: *Boletim de Geociências da Petrobras*, v. 13, p. 7–25.
- Etiope, G., B. L. Ehlmann, and M. Schoell, 2013, Low temperature production and exhalation of methane from serpentinized rocks on Earth: A potential analog for methane production on Mars: *Icarus*, doi:10.1016/j.icarus.2012.05.009.
- Etiope, G., & M. Schoell, 2014, Abiotic gas: Atypical, but not rare: *Elements*, v. 10, p. 291–296, doi:10.2113/gselements.10.4.291.
- Etiope, G., & B. Sherwood Lollar, 2013, Abiotic methane on earth: *Reviews of Geophysics*, v. 51, p. 276–299, doi:10.1002/rog.20011.
- Foulger, G. R., 2018, Origin of the South Atlantic igneous province: *Journal of Volcanology and Geothermal Research*, v. 355, p. 2–20, doi:10.1016/j.jvolgeores.2017.09.004.
- Frost, B. R., & J. S. Beard, 2007, On Silica Activity and Serpentinization: *Journal of Petrology*, v. 48, no. 7, p. 1351–1368, doi:10.1093/petrology/egm021.
- Girard, J.-P., & G. S. Miguel, 2018, Hydrothermal Diagenesis and Reservoir Quality in the Pre-Salt Carbonate-Clastic Series of the Kwanza Basin , Offshore Angola, *in AAPG ACE 2018 Annual Convention & Exhibition*.
- Gunnarsson, I., & S. Arnórsson, 2000, Amorphous silica solubility and the thermodynamic properties of H_4SiO_4 in the range of 0° to 350°C at Psat: *Geochimica et cosmochimica acta*, v. 64, no. 13, p. 2295–2307.
- Herlinger, R., E. E. Zambonato, and L. F. De Ros, 2017, Influence of Diagenesis On the Quality of Lower Cretaceous Pre-salt Lacustrine Carbonate Reservoirs from Northern Campos Basin, Offshore Brazil: *Journal of Sedimentary Research*, v. 87, no. 12, p. 1285–1313, doi:10.2110/jsr.2017.70.
- Huang, R., M. Song, X. Ding, S. Zhu, W. Zhan, and W. Sun, 2017, Influence of pyroxene and spinel on the kinetics of peridotite serpentinization: *Journal of Geophysical Research: Solid Earth*, v. 122, no. 9, p. 7111–7126, doi:10.1002/2017JB014231.
- Katayama, I., I. Kurosaki, and K. Hirauchi, 2010, Low silica activity for hydrogen generation during serpentinization: An example of natural serpentinites in the Mineoka ophiolite complex, central Japan: *Earth and Planetary Science Letters*,

- v. 298, p. 199–204, doi:10.1016/j.epsl.2010.07.045.
- Marcaillou, C., M. Muñoz, O. Vidal, T. Parra, and M. Harfouche, 2011, Mineralogical evidence for H₂ degassing during serpentinization at 300°C/300bar: Earth and Planetary Science Letters, v. 303, no. 3–4, p. 281–290, doi:10.1016/j.epsl.2011.01.006.
- McCollom, T. M., F. Klein, M. Robbins, B. Moskowitz, T. S. Berquo, N. Jöns, W. Bach, and A. Templeton, 2016, Temperature trends for reaction rates, hydrogen generation, and partitioning of iron during experimental serpentinization of olivine: Geochimica et Cosmochimica Acta, v. 181, p. 175–200, doi:10.1016/j.gca.2016.03.002.
- Münntner, O., G. Manatschal, L. Desmurs, and T. Pettke, 2010, Plagioclase peridotites in ocean–continent transitions: refertilized mantle domains generated by melt stagnation in the shallow mantle lithosphere.: Journal of Petrology, v. 51, p. 255–294.
- Neto, E. V. S., J. R. Cerqueira, and A. Prinzhofer, 2012, Origin of CO₂ in Brazilian Basins: AAPG Annual Convention and Exhibition, v. 40969.
- Oufi, O., M. Cannat, and H. Horen, 2002, Magnetic properties of variably serpentined abyssal peridotites: Journal of Geophysical Research, v. 107, no. B5, doi:10.1029/2001JB000549.
- Parkhurst, D. L., and C. A. J. Appelo, 2013, Description of input and examples for PHREEQC version 3 - A computer program for speciation, batch-reaction, one-dimensional transport, and inverse geochemical calculations., *in* U.S. Geological Survey Techniques and Methods: USGS.
- Peters, D., A. Bretscher, T. John, M. Scambelluri, and T. Pettke, 2017, Fluid-mobile elements in serpentinites: Constraints on serpentinitisation environments and element cycling in subduction zones: Chemical Geology, v. 466, no. March, p. 654–666, doi:10.1016/j.chemgeo.2017.07.017.
- Pinto, V. H. G., G. Manatschal, A. M. Karpoff, M. Ulrich, and A. R. Viana, 2017, Seawater storage and element transfer associated with mantle serpentinization in magma-poor rifted margins: A quantitative approach: Earth and Planetary Science Letters, v. 459, no. 12, p. 227–237, doi:10.1016/j.epsl.2016.11.023.
- Poros, Z. *et al.*, 2017, Origin of Silica in Pre-Salt Carbonates , Kwanza Basin , Angola: AAPG Annual Conference and Exhibition, v. 51413, p. 3200.
- Rogerson, M. *et al.*, 2017, Are spherulitic lacustrine carbonates an expression of large-scale mineral carbonation? A case study from the East Kirkton Limestone,

- Scotland: Gondwana Research, v. 48, p. 101–109, doi:10.1016/j.gr.2017.04.007.
- Russell, M. J., A. J. Hall, and W. Martin, 2010, Serpentization as a source of energy at the origin of life: Geobiology, v. 8, no. 5, p. 355–371, doi:10.1111/j.1472-4669.2010.00249.x.
- Saller, A., S. Rushton, L. Buambua, K. Inman, R. McNeil, and J. A. D. Dickson, 2016, Presalt stratigraphy and depositional systems in the Kwanza Basin, offshore Angola: AAPG Bulletin, v. 100, no. 7, p. 1135–1164, doi:10.1306/02111615216.
- Seyfried, W. E., D. I. Fouustoukos, and Q. Fu, 2007, Redox evolution and mass transfer during serpentinization: An experimental and theoretical study at 200°C, 500 bar with implications for ultramafic-hosted hydrothermal systems at Mid-Ocean Ridges: Geochimica et Cosmochimica Acta, v. 71, no. 15, p. 3872–3886, doi:10.1016/j.gca.2007.05.015.
- Seyfried, W. E., N. J. Pester, B. M. Tutolo, and K. Ding, 2015, The Lost City hydrothermal system: Constraints imposed by vent fluid chemistry and reaction path models on subseafloor heat and mass transfer processes: Geochimica et Cosmochimica Acta, v. 163, p. 59–79, doi:10.1016/j.gca.2015.04.040.
- Sherwood Lollar, B., T. D. Westgate, J. A. Ward, G. F. Slater, and G. Lacrampe-Couloume, 2002, Abiogenic formation of alkanes in the Earth's crust as a minor source for global hydrocarbon reservoirs.: Nature, v. 416, p. 522–524.
- Szatmari, P., 1989, Petroleum Formation by Fischer-Tropsch Synthesis in Plate-Tectonics: American Association of Petroleum Geologists Bulletin, v. 73, no. 8, p. 989–998.
- Szatmari, P., T. C. O. da Fonseca, and N. F. Miekeley, 2011, Mantle-like trace element composition of petroleum — contributions from serpentizing peridotites., in D. Closson, ed., Tectonics: InTech, p. 332–358, doi:10.5772/14063.
- Szatmari, P., & E. J. Milani, 2016, Tectonic control of the oil-rich large igneous-carbonate-salt province of the South Atlantic rift: Marine and Petroleum Geology, doi:10.1016/j.marpetgeo.2016.06.004.
- Teboul, P. A., C. Durlet, J. P. Girard, L. Dubois, G. San Miguel, A. Virgone, E. C. Gaucher, and G. Camoin, 2019, Diversity and origin of quartz cements in continental carbonates: Example from the Lower Cretaceous rift deposits of the South Atlantic margin: Applied Geochemistry, v. 100, no. October 2018, p. 22–41, doi:10.1016/j.apgeochem.2018.10.019.
- Teboul, P.-A., J.-M. Kluska, N. C. M. Marty, M. Debure, C. Durlet, A. Virgone, and E.

- C. Gaucher, 2017, Volcanic rock alterations of the Kwanza Basin, offshore Angola - Insights from an integrated petrological, geochemical and numerical approach: *Marine and Petroleum Geology*, v. 80, p. 394–411, doi:10.1016/j.marpetgeo.2016.12.020.
- Thayer, T. P., 1966, Serpentinitization considered as a constant-volume metasomatic process.: *American Mineralogist*, v. 51, p. 685–710.
- Tobie, G., J. I. Lunine, and C. Sotin, 2006, Episodic outgassing as the origin of atmospheric methane on Titan.: *Nature*, v. 440, p. 61–64.
- Tobler, D. J., S. Shaw, and L. G. Benning, 2009, Quantification of initial steps of nucleation and growth of silica nanoparticles: An in-situ SAXS and DLS study: *Geochimica et Cosmochimica Acta*, v. 73, no. 18, p. 5377–5393, doi:10.1016/j.gca.2009.06.002.
- Toft, P. B., J. Arkani-Hamed, and S. E. Haggerty, 1990, The effects of serpentinitization on density and magnetic susceptibility: a petrophysical model: *Physics of the Earth and Planetary Interiors*, v. 65, no. 1–2, p. 137–157, doi:10.1016/0031-9201(90)90082-9.
- Tritlla, J., M. Esteban, R. Loma, A. Mattos, V. Sánchez, C. Boix, P. H. Vieira de Luca, J. Carballo, and G. Levresse, 2018, Carbonates That Are No More: Silicified Pre-Salt Oil Reservoirs in Campos Basin (Brazil): AAPG ACE 2018 Abstracts, no. May.
- Tutolo, B. M., & N. J. Tosca, 2018, Experimental examination of the Mg-silicate-carbonate system at ambient temperature: Implications for alkaline chemical sedimentation and lacustrine carbonate formation.: *Geochimica et Cosmochimica Acta*, v. 225, p. 80–101, doi:10.1016/j.gca.2018.01.019.
- Vils, F., S. Tonarini, A. Kalt, and H. M. Seitz, 2009, Boron, lithium and strontium isotopes as tracers of seawater-serpentinite interaction at Mid-Atlantic ridge, ODP Leg 209: *Earth and Planetary Science Letters*, v. 286, no. 3–4, p. 414–425, doi:10.1016/j.epsl.2009.07.005.
- Wang, G., T. M. Mitchell, P. G. Meredith, Y. Nara, and Z. Wu, 2016, Influence of gouge thickness and grain size on permeability of macrofractured basalt: *Journal of Geophysical Research: Solid Earth*, v. 121, no. 12, p. 8472–8487, doi:10.1002/2016JB013363.
- Warren, J. M., 2016, Global variations in abyssal peridotite compositions: *Lithos*, v. 248–251, p. 193–219, doi:10.1016/j.lithos.2015.12.023.

- Wright, V. P., 2012, Lacustrine carbonates in rift settings: the interaction of volcanic and microbial processes on carbonate deposition: Geological Society, London, Special Publications, v. 370, no. 1, p. 39–47, doi:10.1144/SP370.2.
- Wright, V. P., & A. J. Barnett, 2015, An abiotic model for the development of textures in some South Atlantic early Cretaceous lacustrine carbonates: Geological Society, London, Special Publications, v. 418, no. 1, p. 209–219, doi:10.1144/SP418.3.
- Zalán, P. V, M. do C. G. Severino, C. A. Rigoti, L. P. Magnavita, J. A. B. de Oliveira, and A. R. Vianna, 2011, An Entirely New 3D-View of the Crustal and Mantle Structure of a South Atlantic Passive Margin – Santos , Campos and Espírito Santo Basins , Brazil, *in* AAPG Annual Conference and Exhibition.

CAPÍTULO II – ARTIGO CIENTÍFICO INTERNACIONAL

Introduction

Since the discovery of giant carbonate-hosted oilfields in the Brazilian offshore pre-salt province, its geological evolution has been under debate. These thick Early Cretaceous successions were deposited on the South American and African continental margins during rifting and extension, which culminated with the South Atlantic opening. Distributed stress generated anomalous volcanism on both conjugated margins in zones of active intracontinental lithospheric extension¹. Carbonate deposition was interfingered with multiple lava flows² and intruded by sills and dikes, which may be associated with expressive hydrothermal vents³. These hydrocarbon (HC) reservoirs present gas phases with up to 80% mantellic CO₂ and also He⁴, attesting intense mantle contribution and migration pathways likely related to crustal-scale faults. Such faults have been recognized to reach the mantle, where serpentinization occurs with a progressively lower extent down to 6-8km deep in exhumed portions⁵. This petroleum system was subsequently sealed by basin-wide, locally over 2km-thick, salt accumulations in less than 600 ka⁶. Recent thermodynamic modelling suggests such salts could have been formed by serpentinization-derived hydrothermal brines⁷.

The pre-salt reservoir rocks are characterized by an unusual carbonate ± Mg-smectite ± silica polymorphs mineral assemblage, displaying exotic fabrics and sedimentary textures formed within fresh to progressively more saline and alkaline restricted rift lakes^{8–10}. Lacustrine water likely had high silica contents^{8,10,11} and experiments suggest hyperalkaline pH (10-10.5) must have been required to precipitate spherulitic carbonates and authigenic Mg-clays commonly observed in these reservoirs⁹.

Syn-sedimentary silica and partially to completely silicified and/or dolomitized intervals linked to diagenetic-hydrothermal activity are common in both margins^{12–17}, with carbonate reservoirs exhibiting multiple generations of cements^{12–14,16}. In Campos Basin (Brazil), late silicification is attributed to a high temperature (90-170°C), moderate-high salinity hydrothermal plume coeval with HC migration¹³. Furthermore, intense reservoir fracturing, dissolution, and diagenesis are linked to focused circulation of deep-sourced hydrothermal fluids¹². Similarly, at Kwanza Basin (Angola), reservoirs have undergone anomalously high heat-flows due to fault-controlled high

temperature (150-200°C), CO₂ and HC-bearing brines¹⁶. Also at the Angolan margin, silica precipitated from high temperature (98-123°C), CO₂ and HC-bearing fluids which migrated through faults in combination with carbonate build-ups¹⁷.

Although ubiquitous, the origin of Si and Mg in these rocks is unclear. Some authors evoke weathering and leaching of the Paraná-Etendeka basalts by volcanic catchments^{11,18} and/or alteration of the underlying volcanic basement^{14,15,18,19}. Alternatively, it has been proposed that serpentinization of the exhumed mantle may significantly influence diagenetic dolomitization and silicification in restricted basins²⁰. However, experimental data supporting silica depletion during serpentinization and transport capability by derived fluids is still lacking.

Here we present two sets of serpentinization experiments constraining fluid and mineral chemistry evolution during saline water-peridotite interactions at 230 °C and constant water/rock ratio (4:1) under 13.4 and 20.7 MPa. Such conditions simulate hydration of magma-depleted mantle beneath the pre-salt strata, which was likely developing previously to and synchronously with carbonate reservoir deposition and diagenesis. Our data demonstrates that early serpentinization-fluids are hyperalkaline, Si and Ca-enriched, potentially acting as lithospheric-scale transport agents, which could have influenced sedimentation/diagenesis in various environments throughout Earth's history.

Results

Serpentinization of olivine and orthopyroxene

Rietveld refinement of XRD data demonstrated that all peaks are fully constrained by primary minerals plus lizardite, indicating serpentine is formed in less than 5 days (Fig. 1). No detectable amounts of brucite, magnetite nor other phyllosilicates were observed either by XRD, scanning electron microscopy (SEM), thermogravimetric (TGA) or electron microprobe analyses (EMPA) in any of the runs. Olivine (olv) and orthopyroxene (opx) peak intensities from both pressure series decrease with time, simultaneously with increasing intensities of lizardite peaks (Fig. 1). SEM imaging of Exp.D reveals platy morphology serpentine coating both olivine and orthopyroxene grains, along with rare aggregates of spherical polyhedral serpentine embedded in proto-serpentine (Fig. 2; cf.²¹).

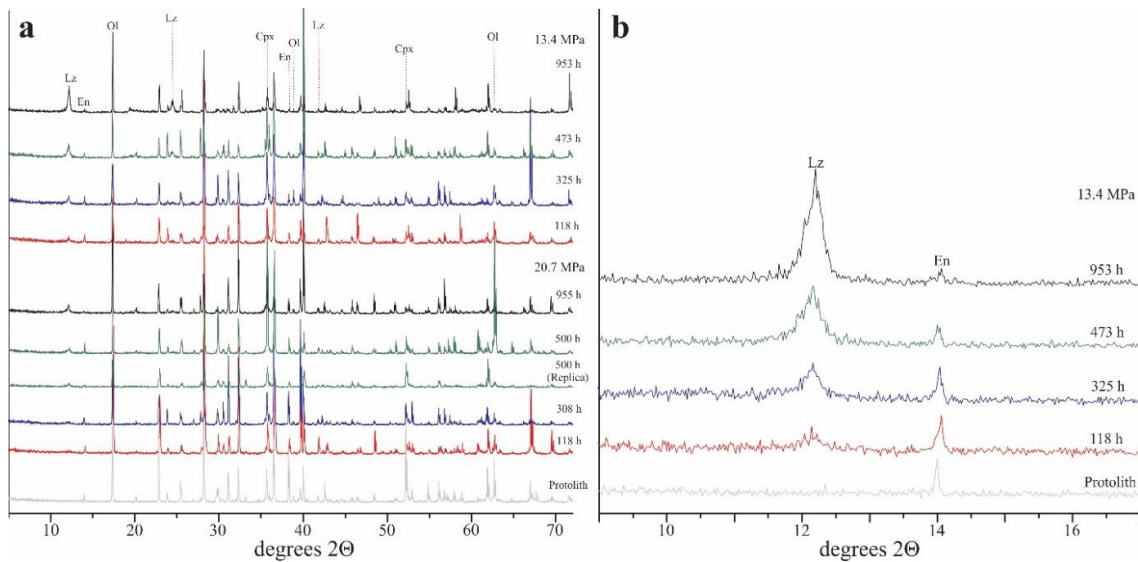


Fig. 1 | Whole rock powder XRD analyses from mantle xenolith PM23 (Protolith) and experimental products. **a**, Lizardite characteristic peaks (12.2 and 24.5°) increase in intensity with reaction time, while no brucite or magnetite peaks are found. Simultaneously, olivine and enstatite peaks decrease over time (e.g. 62.7 and 14° , respectively). **b**, Zoom of the $9\text{--}17$ degrees range of the low-pressure series displaying the progressive intensity decrease in enstatite peak with concomitant increase in lizardite peak. Cpx, clinopyroxene (diopside); En, enstatite; Lz, lizardite; Ol, olivine.

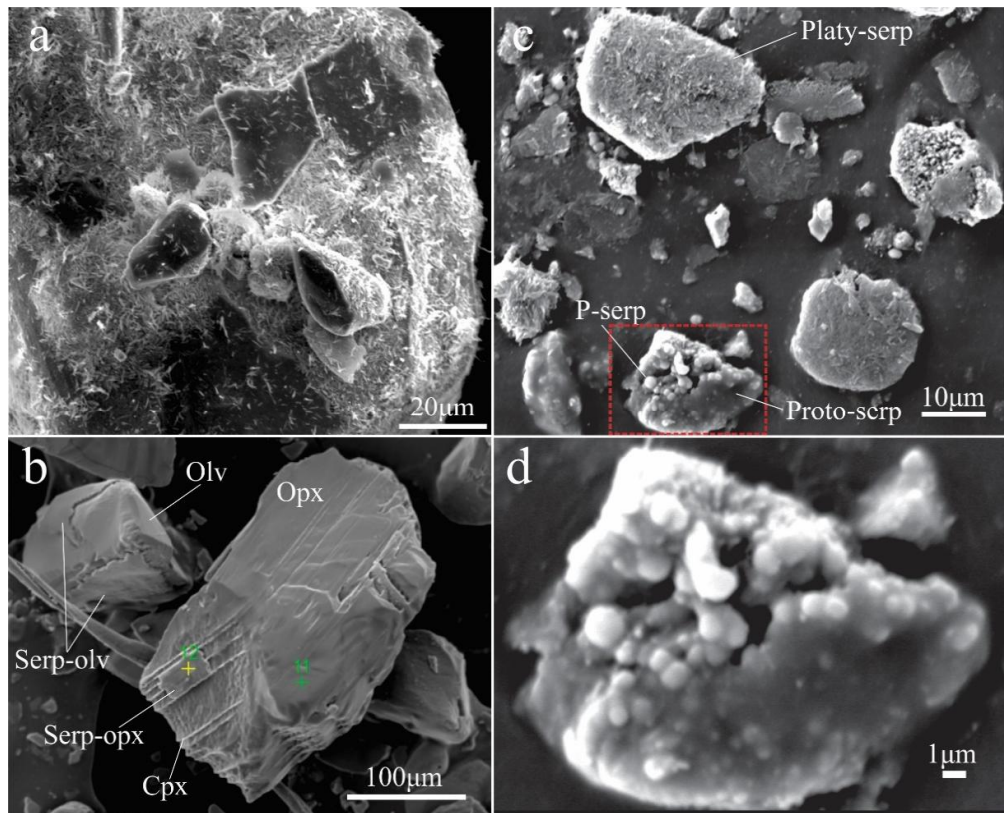


Fig. 2 | SEM secondary electron images (SEI) of untreated, precipitate and supernatant fractions obtained after ultrasonic bath of Exp.D powder in absolute alcohol for 10 minutes. **a**, Untreated sample showing a large olivine grain coated by platy-morphology serpentine. **b**, Precipitate fraction collected after ultrasonic bath featuring partially exposed grains of olivine (olv) and orthopyroxene (opx) covered by derived serpentines. The large opx grain presents various clinopyroxene (cpx) exsolution lamellae which are unaffected by serpentinization. EDS analyses confirm orthopyroxene-derived serpentine (serp-opx, spot 12) is depleted in silica and aluminum relatively to enstatite (spot 11). **c**, Overview of supernatant fraction displaying various grains of platy-serpentine (serp) and rare aggregates of spherical polyhedral serpentine (P-serp) embedded in proto-serpentine (Proto-serp). **d**, Enlarged area marked by the red rectangle in “c”. Aggregate grain exhibiting approximately 1 μm -diameter polyhedral serpentine spheres within an amorphous proto-serpentine matrix.

Serpentinization progress was quantified by loss on ignition (LOI) and TGA (Fig. 3). After 40 days, LOI results estimate ca. 21 and 10 wt% serpentine for the low-pressure series (LPS) and high-pressure series (HPS), respectively, while TGA data reaches similar values of 19 and 10 wt%, respectively. Linear fitting of LOI and TGA data indicates serpentinization rates of 0.57 and 0.52 wt%.day⁻¹ at 13.4 MPa and of 0.25 and 0.28 wt%.day⁻¹ at 20.7 MPa, respectively, which represents ca. 2x slower kinetics with approximately 55% higher vapor-pressure. In addition, the first derivative of TGA data indicates the serpentine dehydration temperature (Fig. 4) shifts from 584.8

to 630.8 °C and from 585.8 to 601.8 °C for the LPS and HPS, respectively. Moreover, smaller peaks of lower temperature (540-550°C) within serpentine dehydration range are observed only in the longest runs (20 and 40 days) of the LPS (Fig. 4).

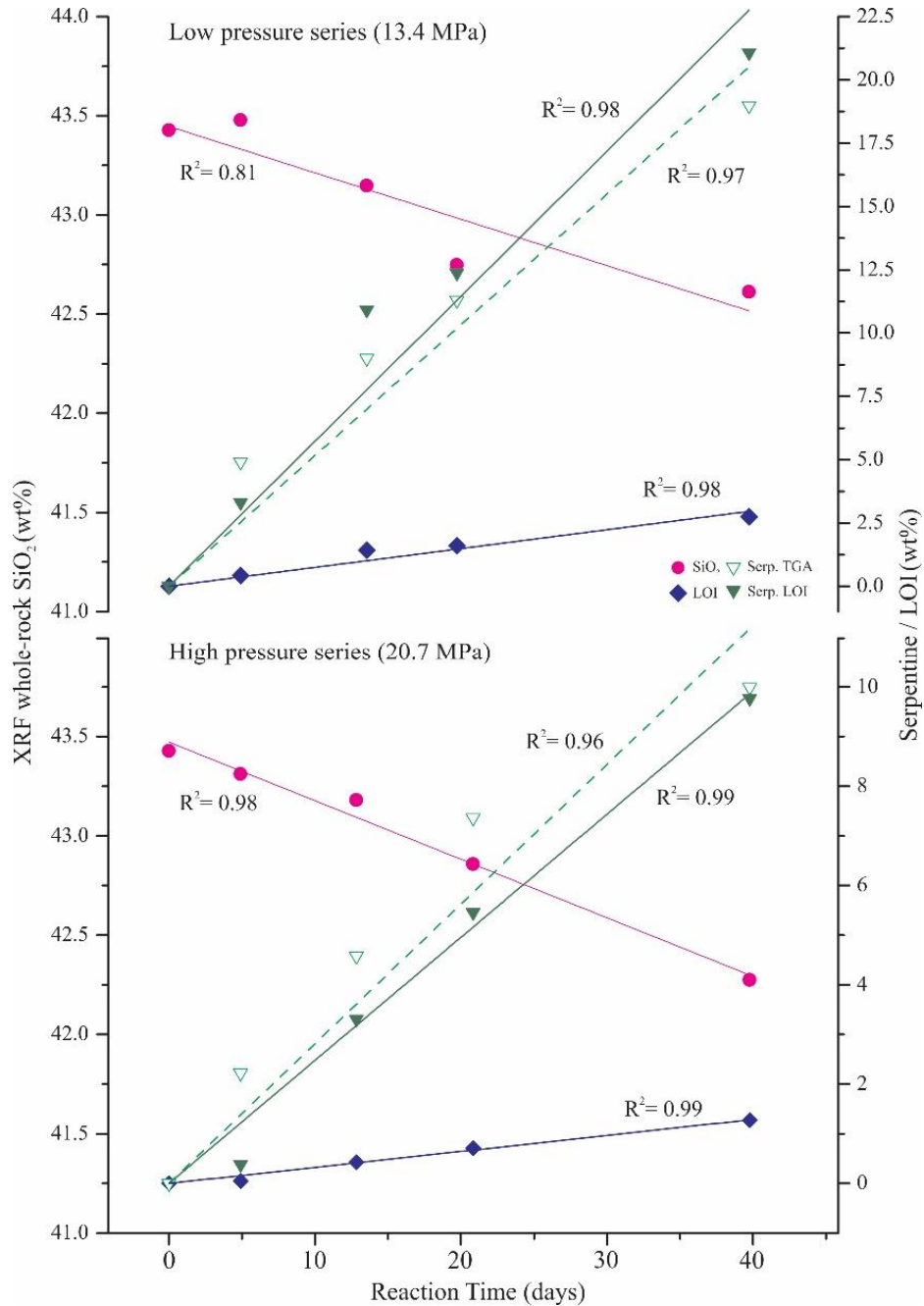


Fig. 3 | X-ray fluorescence (XRF) whole-rock silica, LOI and calculated serpentine content from LOI and TGA considering lizardite as the only hydrated mineral and ideal stoichiometric water (13 wt%). As a phyllosilicate, serpentine is the most prone mineral to be lost during post experiment sample preparation and, thus, these are considered minimum estimates. Fitting of our data (blue line for LOI, olive line for Serp. LOI, green dashed line for Serp. TGA and magenta line for SiO₂) demonstrates that serpentinization/hydration progress and bulk rock SiO₂ depletion are linear.

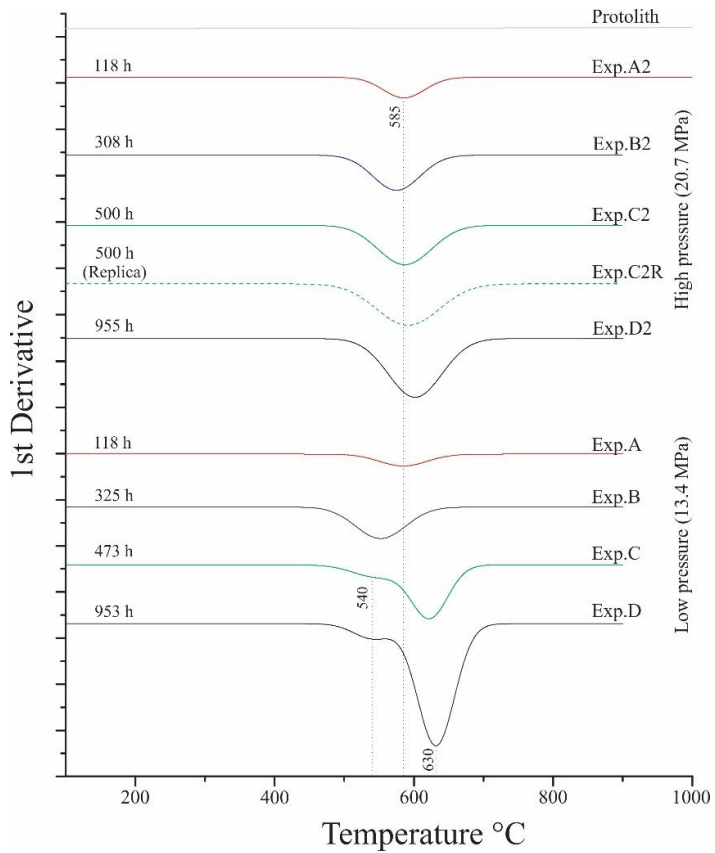


Fig. 4 | The first derivative of thermogravimetric analyses from mantle xenolith PM23 (Protolith) and experimental products. The serpentine peak dehydration temperature increases from the shortest to the longest runs in both experimental sets, except for the two weeks Exp.B and B2 which show lower temperatures. A secondary peak of slightly lower temperature (~540 °C) within serpentine dehydration range is only observed in Exp.C and Exp.D, suggesting the presence of poorly crystalline serpentine. Exp.C2R is the replicate of Exp.C2.

Systematical EMPA illustrates that olivine-derived (serp-olv) and orthopyroxene-derived (serp-opx) serpentines have distinguishable compositions. Spot analyses (Table 2) and quantitative elemental mapping (Fig. 5 & 6a-d) confirm serp-olv Ni/Cr ratios are always $>>2$, while serp-opx never exceeds 0.8, which indicates serpentines reflect their parental mineral Ni/Cr ratios (Tables 1-2). After 5 days, serp-olv has higher Mg/Si and lower Al/Si ratios than serp-opx (Fig. 5 & 6e,f). However, as reaction proceeds, Mg/Si and Al/Si ratios of both serpentines exponentially converge to 1.39 ± 0.04 and 0.04 ± 0.01 , respectively (LPS), and to 1.27 ± 0.05 and 0.04 ± 0.01 , respectively (HPS), after 40 days (Fig. 5 & 6e,f). In addition, serpentines formed under 13.4 MPa have lower average SiO₂ contents (ca. 38 wt%) than serpentines formed at 20.7 MPa (ca. 41 wt%) after 40 days. Analogously, initially formed serp-olv has excess magnesium, total octahedral cations (t.o.c.) >3 apfu and

positive-charge, while serp-opx is magnesium poor and t.o.c. deficient (<3 apfu) (Fig. 5 & 6g). At the end of each series, magnesium concentrations are similar and both serpentines converge to near ideal stoichiometry (3 apfu) under low-pressure, but remain slightly below (2.91 apfu) at higher pressures (Fig. 5 & 6g). Additionally, stoichiometric constrains also demonstrate that, after 40 days, aluminum in both serpentines is mainly tetrahedrally coordinated at 13.4 MPa, whereas it exclusively occupies octahedral sites at 20.7 MPa. Furthermore, charge-balance suggests the two serpentines accommodate variable amounts of Fe^{3+} , with ferric iron being exclusively octahedral in serp-opx, while in serp-olv it is initially tetrahedral and becomes exclusively octahedral after 40 days for both pressure sets (Table 2). Chlorine was likewise incorporated by both serpentines and tends to be depleted with reaction progress regardless of pressure.

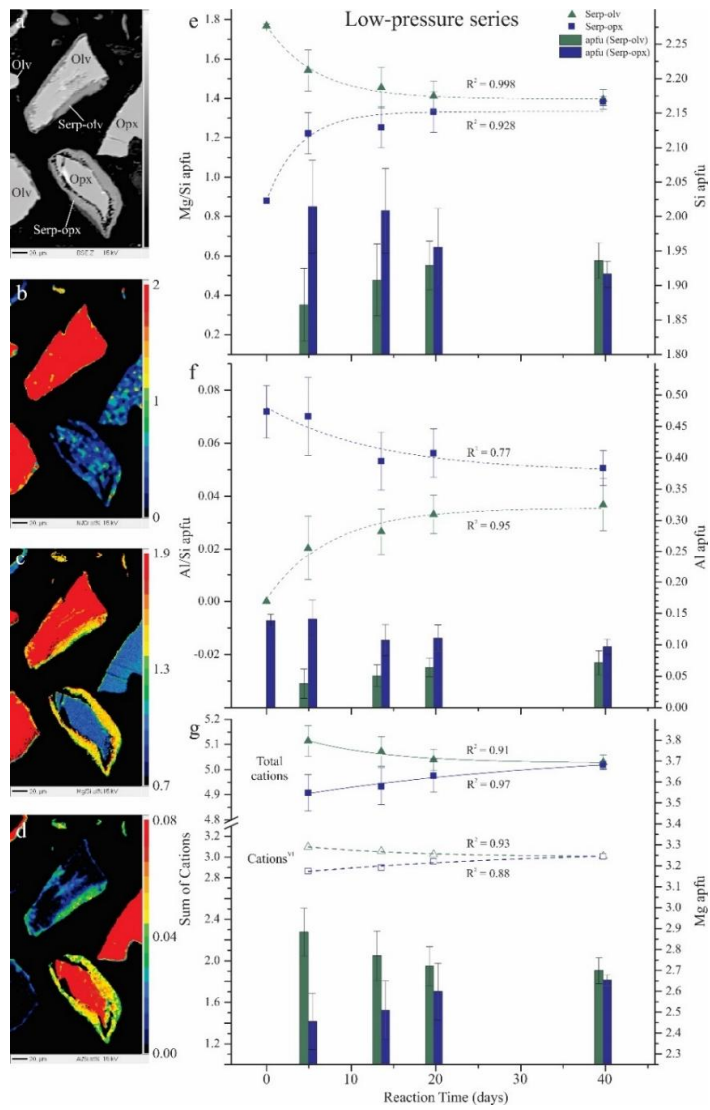


Fig. 5 | a-d, EMP atomic ratio maps of serpentinized peridotite after 40 days at 13.4 MPa (Exp.D). **e-g,** Chemical evolution of serpentines at 13.4 MPa ($n = 114$). Triangles and squares are plotted on the left axis; bars are plotted on the right axis (considering 7, 6 and 4 Oxygens for serpentine, pyroxene and olivine, respectively). Time zero values correspond to parent minerals and, where not visible, error bars (standard deviations) are smaller than symbols. Curves are exponential fits of data. **a,** Backscattered electron image of partially serpentinized olivine and enstatite grains. **b,** Ni/Cr map displaying homogeneous distribution between parent minerals and derived serpentines. **c,** Mg/Si map showing orthopyroxene and olivine-derived serpentines have higher and lower ratios than parent minerals, respectively. Serp-opx has average 37.84 wt% SiO₂, indicating enstatite has lost 30-35% of its silica (Supplementary Tables 1-2). **d,** Al/Si map evidencing orthopyroxene and olivine-derived serpentines have lower and higher ratios relatively to parent minerals, respectively. Serp-opx has average 1.62 wt% Al₂O₃, demonstrating enstatite has lost 49-59% of its aluminum. Although olivine is devoid of Al, serp-olv has average 1.18 wt% Al₂O₃ (Supplementary Tables 1-2). **e,** Initially different Mg/Si ratios and Si apfu of both serpentines exponentially converge after 40 days, with silicon below ideal stoichiometry (<2 apfu). **f,** Initially different Al/Si ratios and Al apfu of both serpentines exponentially converge after 40 days. **g,** Initially different sum of total and octahedral cations (Cations^{VI}) and Mg apfu of both serpentines exponentially converge after 40 days; Notice scale break.

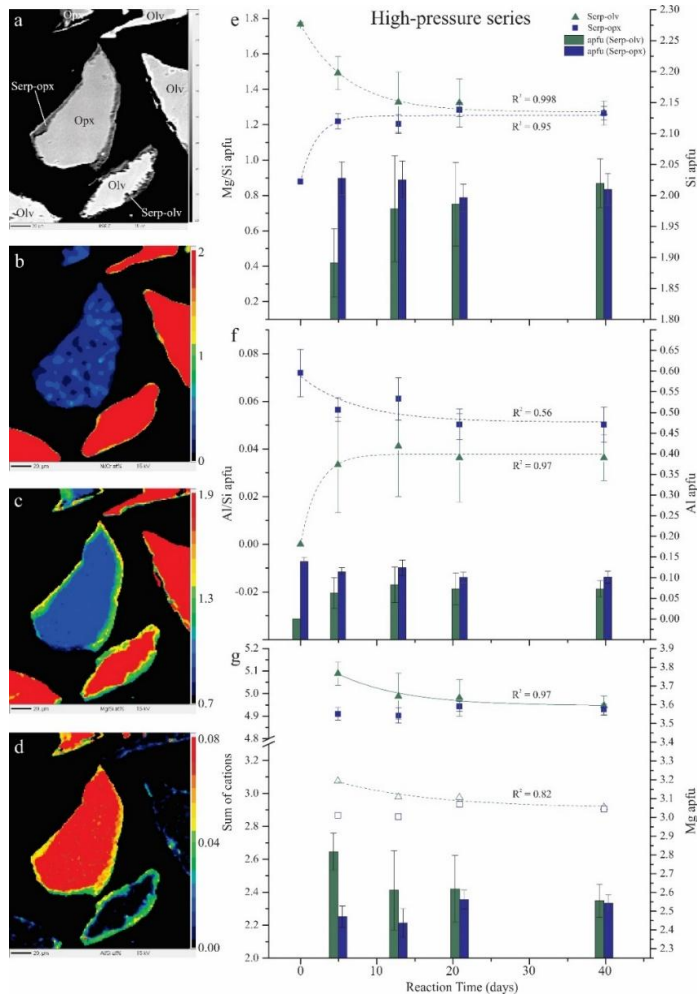


Fig. 6 | **a-d**, EMP atomic ratio maps of serpentinized peridotite after 40 days at 20.7 MPa (Exp.D2). **e-g**, Chemical evolution of serpentines at 20.7 MPa ($n = 184$). Triangles and squares are plotted on the left axis; bars are plotted on the right axis (considering 7, 6 and 4 Oxigens for serpentine, pyroxene and olivine, respectively). Time zero values correspond to parent minerals and, where not visible, error bars (standard deviations) are smaller than symbols. Curves are exponential fits of data. **a**, Backscattered electron image of partially serpentinized olivine and enstatite grains. **b**, Ni/Cr map displaying homogeneous distribution between parent minerals and derived serpentines. **c**, Mg/Si map showing orthopyroxene and olivine-derived serpentines have higher and lower ratios than parent minerals, respectively. Serp-oxp has average 41.76 wt% SiO_2 , indicating enstatite has lost 23-28% of its silica (Supplementary Tables 1-2). **d**, Al/Si map evidencing orthopyroxene and olivine-derived serpentines have lower and higher ratios relatively to parent minerals, respectively. Serp-oxp has average 1.78 wt% Al_2O_3 , demonstrating enstatite has lost 41-57% of its aluminum. Although olivine is devoid of Al, serp-olv has average 1.24 wt% Al_2O_3 (Supplementary Tables 1-2). **e**, Initially different Mg/Si ratios and Si apfu of both serpentines exponentially converge after 40 days, with silicon approaching ideal stoichiometry (2 apfu). **f**, Initially different Al/Si ratios and Al apfu of both serpentines exponentially converge after 40 days. **g**, Initially different sum of total and octahedral cations ($\text{Cations}^{\text{VI}}$) and Mg apfu of both serpentines exponentially converge after 40 days; Notice scale break.

Dissolution of clinopyroxene and spinel

None of the experimental runs evidenced serpentine enveloping clinopyroxene (cpx), although rare dissolution features were observed (Fig. 7). Additionally, when enstatite displays eventual cpx exsolution lamellae, only opx reacts to form serpentine (Fig. 8). Contrarily, spinel grains of all runs often display extensive dissolution features (Fig. 9). EMP element maps show that, after 40 days, spinel rims have lost around 30–45 % of their initial Al_2O_3 and are enriched in the other analyzed elements (Fig. 9 and Table 1).

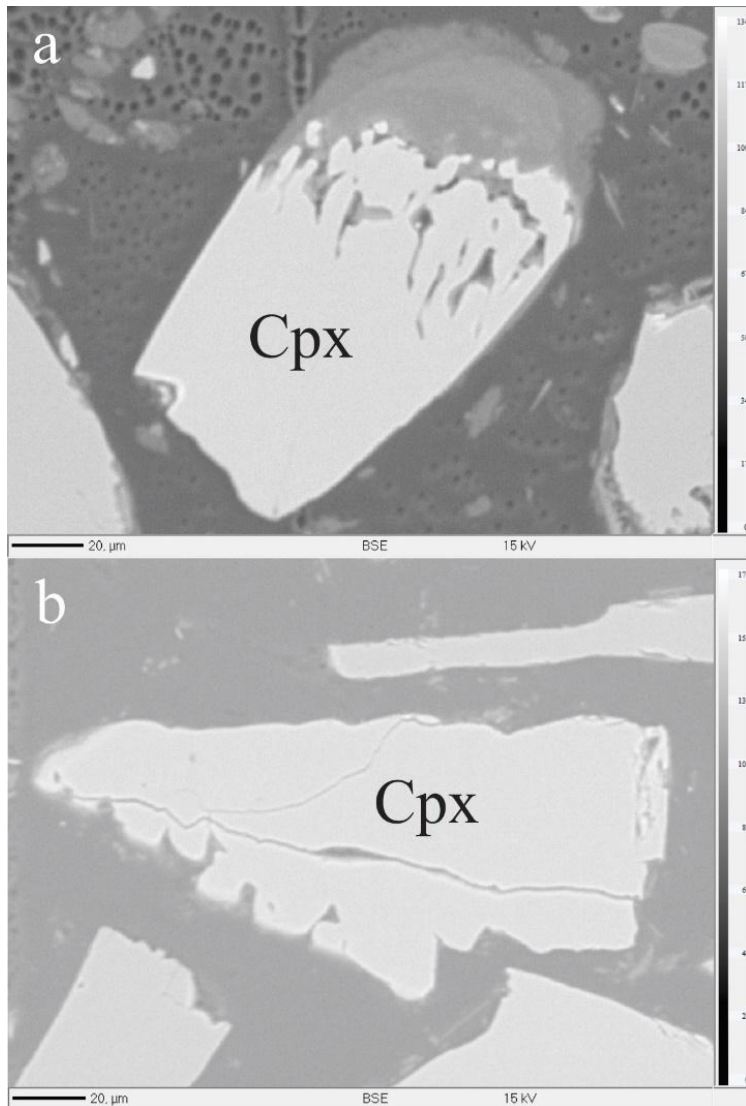


Fig. 7 | Backscattered electron images of diopside (cpx) grains with rare dissolution features. **a**, Partially dissolved clinopyroxene grain after ca. 20 days at 13.4 MPa (Exp.C). Darker grey area on the top right of the grain is a portion of the same mineral which was not exposed by polishing. **b**, Diopside grain displaying dissolved edges after only approximately 5 days at 20.7 MPa (Exp.A2).

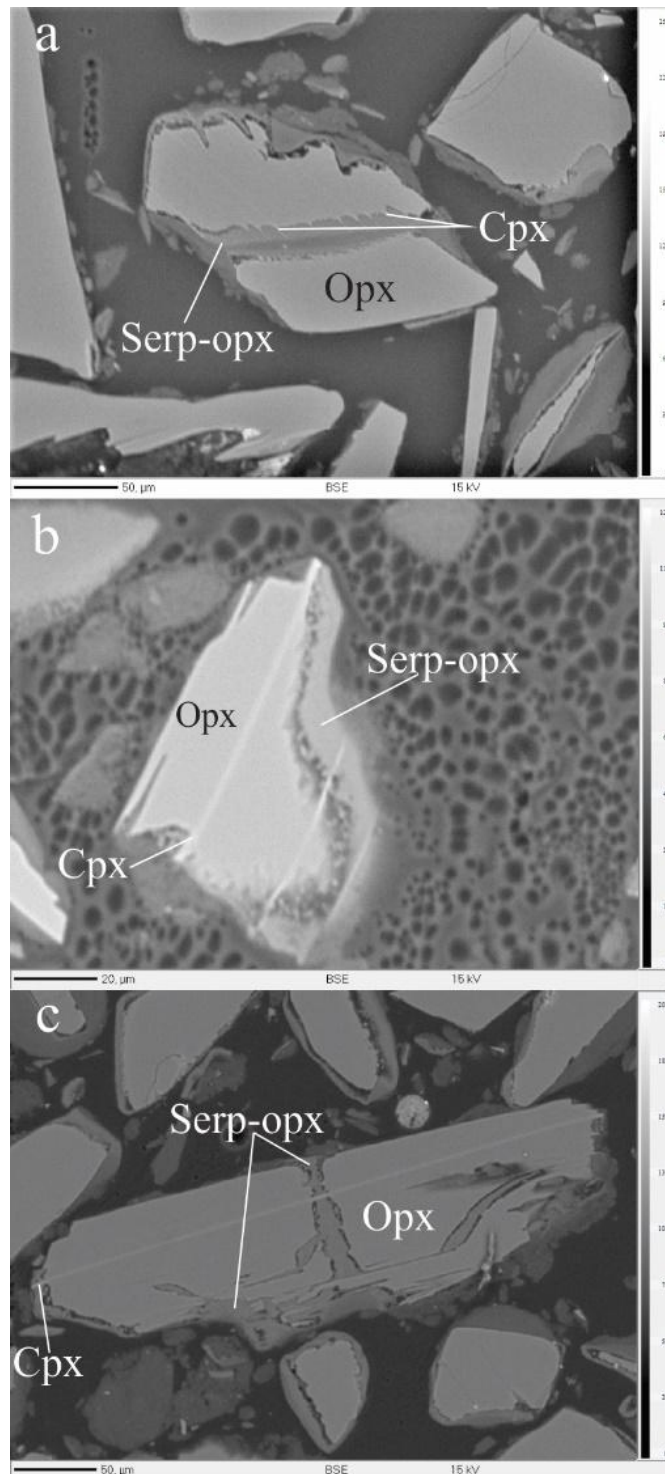


Fig. 8 | Backscattered electron images of partially serpentinized enstatite (opx) grains with sub micrometer-thick diopside (cpx) exsolution lamellae (lighter grey/whitish color) unaffected by newly formed lizardite (serp-opx) in fractures and around orthopyroxene grains. **a**, Multiple cpx exsolution lamellae form resistant cusps traversing newformed serpentine in a fracture which divides a larger opx crystal (Exp.C). **b**, Whitish cpx lamellae unaffected by enveloping serp-opx (Exp.D) **c**, Light grey diopside exsolution lamellae unaffected by serpentines formed around and within fractures in enstatite. Serpentinization follows fractures and crystallographic planes in orthopyroxene (Exp.D).

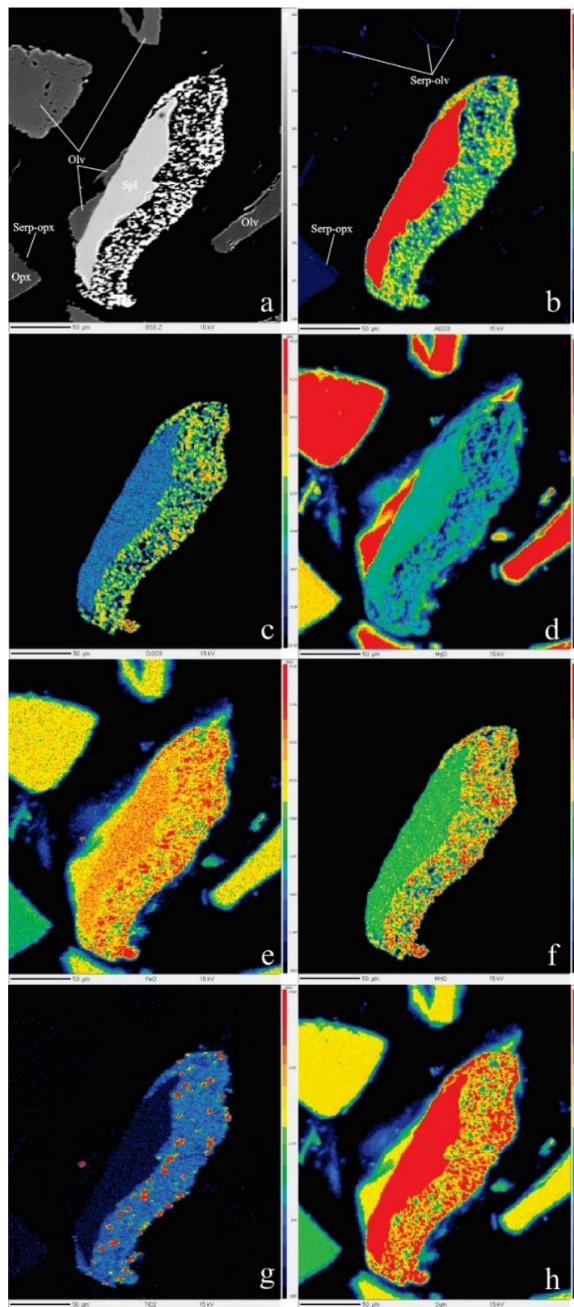


Fig. 9 | EMP backscattered electron (BSE) image and quantitative element maps of an extensively dissolved spinel (Spl) crystal from Exp.D2. **a**, BSE image of a spinel grain presenting a wide dissolution rim. Olivine (olv), enstatite (opx) and derived serpentine (Serp-opx) are also visible in the frame. **b**, Al₂O₃ map displaying spinel dissolution rim has 27.7 to 34.7 wt% aluminum oxide, which amounts to a 30-45% loss of their initial aluminum content (Table 1). Olivine derived serpentine (serp-olv) and serp-opx are also highlighted. **c**, Cr₂O₃ map showing chromium is concentrated at the rim relatively to core. **d**, MgO map evidencing that magnesium concentration is only slightly concentrated at the edges of the dissolution rim and of the relict crystal. **e**, FeO map (total iron) illustrating iron is concentrated at the rim relatively to core. **f**, MnO map displaying manganese is highly concentrated at the rim relatively to the core, reaching approximately 4 wt%. **g**, TiO₂ map exhibiting titanium is concentrated at the rim relatively to core. High concentration spots within the dissolved rim possibly correspond to nucleation loci. **h**, Total oxides sum map.

Whole-rock geochemistry, mass-volume increase and serpentinization-derived fluids

Whole-rock XRF analyses of the starting peridotite and serpentized products of all experiments are presented in Table 3. The results demonstrate a linear SiO_2 depletion of the serpentized products compared to the starting peridotite (Fig. 3). At 13.4 MPa, depletion rate is $5.33 \times 10^{-2} \text{ \%}\cdot\text{day}^{-1}$ of the initial silica content, while at 20.7 MPa it reaches $6.43 \times 10^{-2} \text{ \%}\cdot\text{day}^{-1}$, which corresponds to >20 % faster loss at higher pressure (Fig. 3). Similarly, MgO and CaO are also depleted, whereas Fe_2O_3 , NiO and Cr_2O_3 remain virtually constant and MnO , TiO_2 and Al_2O_3 are highly enriched with reaction progress. As SiO_2 , MgO and CaO are replaced by H_2O , rock density decreases with serpentinization progress^{20,22–24}. Complementarily, the dry masses of serpentized products from the LPS and HPS progressively increased 0.69-1.60 % and 0.34-1.30 % in comparison with initial peridotite masses, respectively, implying volume expansion. Applying density-serpentinization degree correlations²⁰ to our data, we observed a linear volume increase with serpentine content ($y = +0.35088x$), reaching +6.77 % at 21 wt% serpentine (Fig. 10).

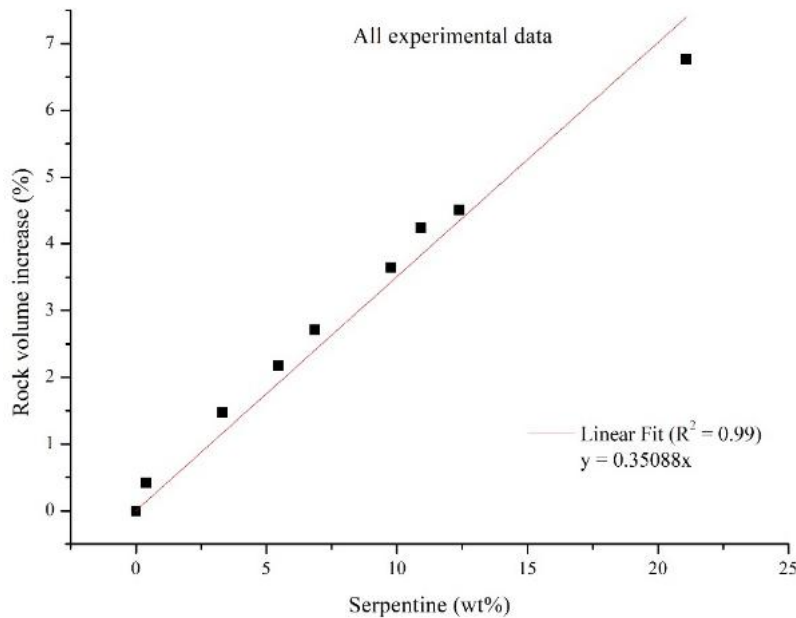


Fig. 10 | Rock volume increase as a function of serpentine wt% for both pressure sets. Initial volumes were calculated assuming average peridotite density (3.2873 g/cm^3), while volumes of serpentized products were calculated by applying the density-serpentinization degree empirical formula ($\rho = -0.761x + 3.2873$) of Pinto *et al.* 2017 (and references therein), where “x” represents our estimated serpentine content from LOI. Our data results in a positive linear correlation between rock volume and serpentization. Additionally, low- and high-pressure experiments (A and B2), which both contain 3.31 wt% serpentine, resulted in a nearly identical volume increase of +1.47 and +1.50 %, respectively, demonstrating volume expands regardless of pressure and excellent agreement of data. Furthermore, considering fully serpentized peridotites contain on average 90 wt% serpentine, 7 wt% magnetite and 3 wt% brucite, our results suggest rock volume increases over 31.5% upon reaction completion, in agreement with previous estimates.

Analyses of the starting solution and serpentization-derived fluids/gases of all runs are shown in Table 4. Initial solution pH (6.0) exponentially rises and tends to stabilize around 11.3 and 10.7 for the LPS and HPS, respectively (Fig. 11). Serpentization fluids become variably but consistently Ca-enriched (0.31-1.22 mmol/kg), while Al, Cr, Mn and Ni were always below the detection limit. Iron (39.28 $\mu\text{mol}/\text{kg}$) and magnesium (0.40 mmol/kg) were only detected in Exp.A. Dissolved silicon reaches the highest concentration in 5 days runs of the LPS ($>226.36 \mu\text{mol}/\text{kg}$) and HPS (197.27 $\mu\text{mol}/\text{kg}$), progressively decreasing to 9.58 and 83.38 $\mu\text{mol}/\text{kg}$ after 40 days, respectively (Fig. 11). However, XRF whole-rock SiO_2 mass-balance of solids pre- and post-experiments suggests that under 20.7 MPa/230 °C fluids become silica-supersaturated in less than 40 days, attaining increasingly higher concentrations with serpentization progress in both series (Fig. 11). Such constrains suggest that most

silica precipitated from the solution before ICP-OES analyses. Ion chromatography showed fluctuating chlorinity, with LPS and HPS presenting lower to equivalent (512.25-545.05 mmol/kg) and higher concentrations (567.60-601.93 mmol/kg) than the starting solution, respectively. Fluids often exhibited exsolving bubbles even several hours after sampling, indicating solutions were gas saturated. Gas chromatography of the high-pressure experiments indicates that CH₄ was formed in all analysed runs (B2-D2), and its concentration increases from 6.52 to 39.83 ppm. Similarly, CO₂ concentration increases from 11.7 to 322 ppm, while H₂ (ca. 100 ppm) was only detected in the longest run.

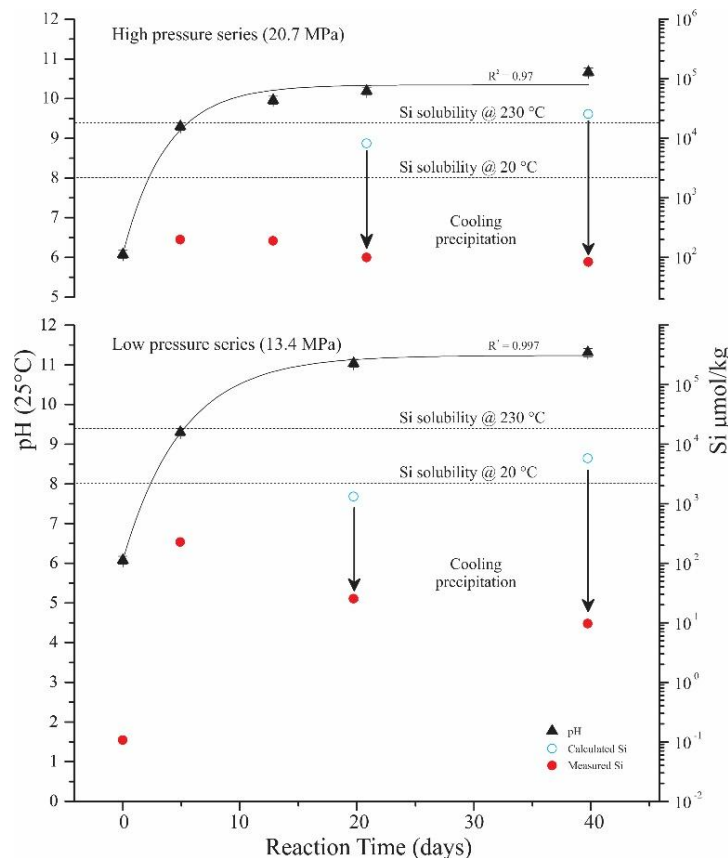


Fig. 11 | Measured and calculated aqueous Si concentration and pH evolution through experiments. Expected aqueous silicon concentration was calculated by subtracting the measured water mass of reaction products (LOI) from the initial input solution mass, in conjunction with pre- and post-experiment whole-rock XRF SiO₂ mass-balance. The measured pH_{25°C} increases exponentially and after 20 days tends to stabilize around 11.3 and 10.7 for the LPS and HPS, respectively. Our estimations suggest that at 20.7 MPa serpentinization fluids become Si-supersaturated in less than 40 days and, upon cooling to room temperature, nucleate (black arrows) most aqueous Si as silica nanoparticles. This behavior therefore results in progressively lower measured Si_(aq) concentrations as fluids become more saturated. Error bars are standard deviations of duplicate analyses and, where not visible, are smaller than symbols. Starting solution Si concentration is equal for both sets. Silica solubility values from experimental data²⁵.

Discussions and Conclusions

Understanding serpentinization in two steps

The slower reaction kinetics observed under higher pressure is likely consequence of reduced permeability/reaction surface area with increased effective pressure on peridotite powder, consistent with overburden-effects on coarse-grained fault gouges²⁶. These results suggest serpentinization degree along fault planes are significantly reduced with increasing depth (overburden-pressure), in agreement with mantle serpentinization estimates of the Santos Basin⁵. Compared to other peridotite serpentinization experiments at 300 °C/30 MPa (1 µm grain size)²⁷ and 311 °C/300 MPa (100-177 µm grain size)²⁸, our results show slower reaction rates in consequence of larger initial grain size and lower temperature.

Lizardite formation and the absence of magnetite in our experiments are consistent with the mineralogy observed in low temperature (<300 °C) serpentinites²⁹ and at low serpentinization degrees^{22–24,30}. Detailed EMP characterization reveals that enstatite and olivine serpentinization are intrinsically coupled, as Al and Si are transferred from serp-opx to serp-olv, while the opposite is true for Mg. Such mass transfer of silica and aluminum has been previously reported by other experimental²⁸ and modeling studies³¹ in response to strong geochemical potential gradients developed during olv and opx simultaneous serpentinization. Our data show that the concentration of major elements, Mg/Si and Al/Si ratios of serp-olv and serp-opx stabilize after 40 days, and that the Ni/Cr ratio can reliably identify the parent mineral. Since olivine and the starting solution are nominally devoid of aluminum and chromium, higher variability of Al/Si and Ni/Cr ratios in serp-olv suggests the incorporation of Al and Cr from dissolved spinels, which accelerates reaction rates²⁸. Furthermore, cation exchange between serp-olv and serp-opx is affected by pressure, as Al is preferentially tetrahedral under 13.4 MPa and exclusively octahedral at 20.7 MPa, resulting in lower Si (<2 apfu) and, therefore, higher Mg/Si ratios at lower pressures. Silica mobility is also favored with increased pressure, as Mg/Si ratios of both serpentines converge faster at 20.7 MPa (Supplementary Fig. 4), which is consistent with higher average silica in high-pressure serpentines and our Si_(aq) calculations (Fig. 3). Similarly, initially tetrahedral ^{(IV)Fe³⁺ in serp-olv reflects its parent-inherited Si-deficiency, which is progressively supplemented by Si and Al from pyroxenes and spinels, dislocating Fe³⁺ to octahedral sites. Such observations imply that Fe³⁺ in serp-olv would only remain tetrahedral in the absence of pyroxenes and spinels, suggesting the reported rise by}

Marcaillou *et al.*²⁷ after ~77% reaction extent is related to olivine-only serpentinization. Complementally, proto and polyhedral serpentine only observed in the longest runs (Exp.C and D) represent the latest stage of enstatite hydration at temperatures <200–300 °C²¹. In addition, the increasing dehydration temperatures of lizardite on TGA are likely due to the substitution of trivalent cations for magnesium and silicon, which increase lizardite thermal stability³².

Our results imply that clinopyroxene is not a serpentine precursor, likely attributable to its very low Mg/Si ratio (0.41 – Table 1) and possibly because Ca²⁺ cannot be accommodated by serpentine octahedral sites, being released into serpentinization-fluids. This conclusion is also supported by unaltered cpx in highly serpentinized natural samples³³ and cpx increased abundance relative to primary minerals after experimental Iherzolite serpentinization³⁰. At our experimental conditions diopside and spinel are hydrothermally dissolved, mainly releasing Ca, Al and Cr into serpentinization-derived fluids^{27,28,30,34}. Moreover, since no magnetite was detected in our experiments, H₂ synthesis from water was probably spinel-catalyzed³⁵, which presupposes Fe⁺² oxidation and Fe³⁺ incorporation by serpentine, in agreement with our calculated stoichiometry and previous reports^{30,33}. The methane concentration increase throughout our analysed runs is likely linked to metal-catalyzed Fischer-Tropsch-Type carbon dioxide hydrogenation (CO₂ + 4H₂ = CH₄ + 2H₂O), commonly associated with serpentinized ultramafic rocks³⁶. Assuming this methane-forming mechanism implies that H₂ was also generated in all runs. We suggest that H₂ produced during initial serpentinization was fully consumed by CO₂ to form methane, while after 40 days its production exceeded CO₂ methanation. In addition, carbon dioxide concentrations approach atmospheric levels (294-350 ppm) within 40 days, suggesting dissolved CO₂ was the major source of carbon. In summary, within 6 weeks our experimental-fluids attained comparable pH, silica concentration range and chlorinity to those of the Lost City Hydrothermal Field^{37,38} (LCHF), where subseafloor serpentinization occurs at 200 ± 50 °C³⁹. Besides, our fluids present methane, H₂, low-Mg concentration and Ca-enrichment also observed at the LCHF, which suggests it is a natural analogue of our experiments. Furthermore, serpentinization-derived experimental-fluids also resemble the pH, moderate-calcium and low-magnesium concentrations of those of Si-rich pre-salt lake waters⁹, suggesting our fluids could, in theory, precipitate spheroidal CaCO₃ and Mg-silicates at conditions analogous to depositional environments of HC-reservoirs.

The verified whole-rock silica depletion accompanying peridotite serpentinization progress is in agreement with previous studies of natural and modeled serpentinization^{20,40} and compiled data (Table 1). As silica, magnesium and calcium are depleted from the rock, manganese, titanium and specially aluminum are relatively concentrated, remaining immobile during serpentinization. However, although immobile on rock-scale, our data show that during peridotite hydration Al is mobile on the mineral-scale. Furthermore, using our compiled average SiO₂ concentrations, observed volume expansion rate, peridotite density of 3.2873 g/cm³ and considering average serpentinites ($\rho = 2.7536 \text{ g/cm}^3$) contain 90 wt% serpentine, 7 wt% magnetite and 3 wt% brucite, we estimate approximately 1% of peridotite mass is released as silica_(aq). Which means that hydration of 1 m³ of peridotite would result in 1.31 m³ of serpentinite (>31.5 % volume increase) and circa 33 kg of aqueous silica upon reaction completion (<6-12 months), demonstrating serpentinization is neither isovolumetric nor isochemical, but geologically instantaneous. This mass-balance suggests early-stage serpentinization immediately releases abundant silica into derived fluids.

Previous experimental data demonstrates that upon cooling of silica-rich fluids from 230 to 30-60 °C, approximately 80% of the initial SiO_{2(aq)} polymerizes within 20 minutes, regardless of final temperature⁴¹. Initial aqueous SiO₂ concentration is the prime control for the rate of silica polymerization and nanoparticle growth⁴¹, meaning that silica-over-supersaturated fluids will precipitate more and faster than less silica-supersaturated ones. Therefore, hydrothermal solutions with progressively higher initial SiO_{2(aq)} contents will result in fluids with progressively lower final aqueous silica concentrations upon cooling to room temperatures due to precipitation of silica-nanoparticles⁴¹. Such behavior illustrates why our measurements in serpentinization-fluids present “decreasing” Si_(aq) concentrations with reaction progress, as also previously reported^{30,42}. The results of Tobler&Benning⁴¹ in conjunction with this study suggest that published Si concentrations in high pH fluids from serpentinite-hosted hydrothermal fields (e.g. LCHF³⁸) may be highly underestimated. Rapid cooling to seafloor temperatures (1-3°C) and long time-lapse between sampling and onshore analyses probably precipitated most silica that was originally in solution.

In summary, combining our results with previous studies²²⁻²⁴, peridotite serpentinization can be understood as a multi-reaction 2-stage hydration process. Here we present a comprehensive new model fully described in Figure 12, based on this study and literature^{22-24,28,30,33,34,36,40,42}.

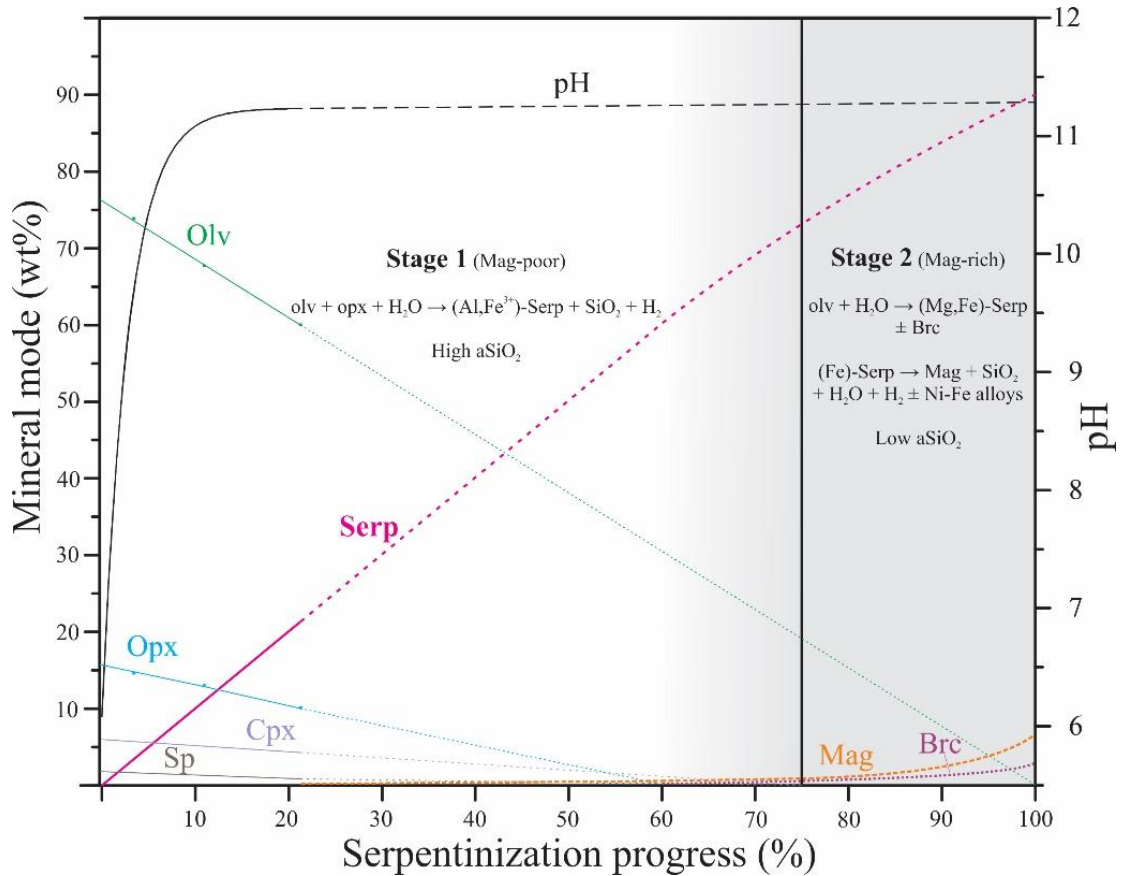


Fig. 12 | Schematic peridotite serpentinization model in two stages. Our data is represented by full lines, while dashed lines are extrapolations based on literature. The first stage was addressed by our experiments and previous ones²⁸, being characterized by simultaneous generation of Al-rich serpentine after orthopyroxene and olivine. Fluid pH rises and stabilizes (>10), enabling excess $\text{SiO}_{2(\text{aq})}$ to migrate upwards due to open fluid circulation, while clinopyroxene and spinel are fully dissolved. Only traces of brucite and magnetite may form due to elevated aluminum and silica activities ($a\text{SiO}_2$), with spinel-catalyzed H_2 production linked to Fe^{3+} incorporation by serpentine. The second phase is characterized by olivine hydration resulting in Mg-rich serpentine \pm brucite^{33,34,42}. This stage has remarkably low $a\text{SiO}_2$, favoring brucite stability and the breakdown of the iron-component of serpentine into magnetite + silica + water + H_2 ^{34,40}. Besides promoting silica impoverishment and magnetite-controlled H_2 , destabilization of serpentine can precipitate Ni-Fe alloys³⁴, likely associated with Ni-rich serp-olv. Furthermore, serpentinites latest textural features comprise exclusive replacement of relict olivine³³ by serpentine-poor magnetite-rich veins associated with Ni-Fe alloys⁴⁰. Additionally, under adequate PT conditions such alloys may catalyze CO_2 hydrogenation³⁶, enhancing methanogenesis. As peridotites contain 60% maximum modal pyroxenes, magnetite-poor stage one fits with up to 60-75% reaction progress^{23,24,33}, after which olivine-only late-stage serpentinization exponentially produces magnetite^{22-24,30,33}. Duration of each stage depends on peridotite modal composition, implying that olivine-richer lithotypes have increasingly longer second stages and slower rates. Brc, brucite; Mag, magnetite; Sp, spinel.

A mantle influenced petroleum system: The South Atlantic pre-salt

The South Atlantic opening proceeded via intermittent tectonic and largely mafic volcanic activity during its rifting, which produced gases such as CO₂ and H₂S. Massive prolonged carbon emissions at the African Rift Valley indicate magma chambers at the Moho source mantellic-CO₂ and likely other fluids/gases (He) to rift basins and atmosphere through crustal-deep faults, even during inactive rifting⁴³. Alternating with major volcanic events, momentaneous tectonic quiescence enabled fault-controlled water percolation to reach residual peridotites, triggering widespread serpentinization. Here we propose the model in Figure 13 to describe these events and processes.

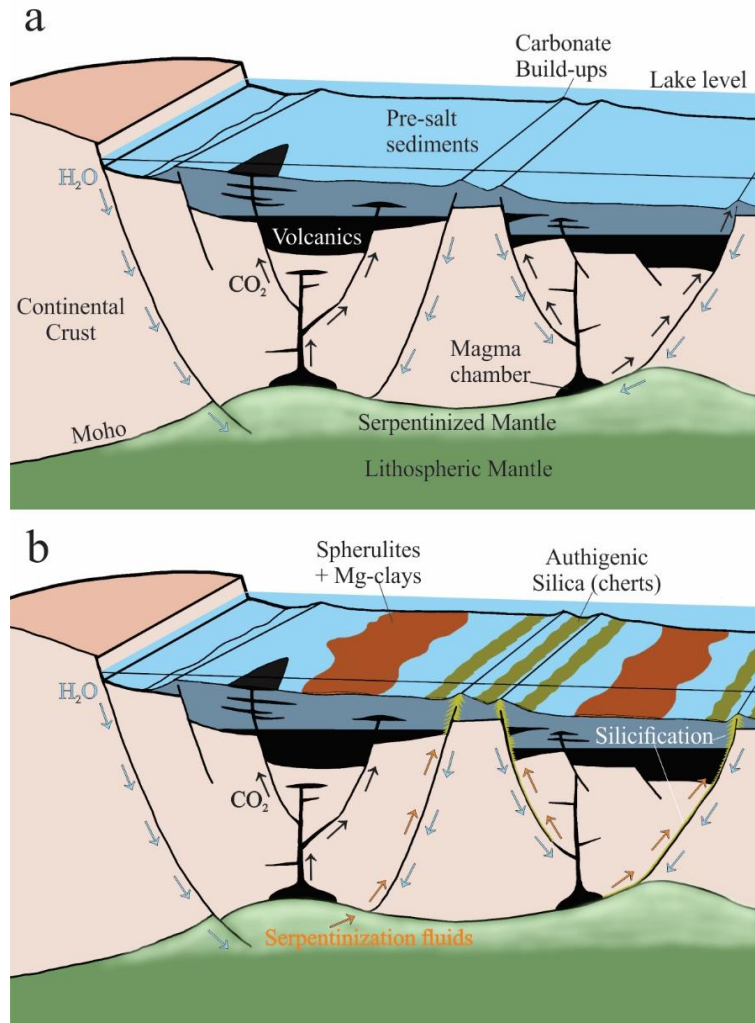


Fig. 13 | Schematic model of the influence of serpentinization-derived fluids on the South Atlantic pre-salt province (not to scale). **a**, Fault-controlled downward water percolation (blue arrows) following major volcanism triggers the serpentinization of residual mantle peridotites. Magma chambers at the base of the hyperextended continental crust (<5-10 km-thick cf.⁵) continuously supply CO₂ (black arrows) to the basin through faults/fractures and seepage, facilitating carbonate deposition. **b**, Serpentinization-derived hyperalkaline fluids enriched in silica, calcium, methane and hydrogen generate moderate-high temperature (200-300°C) hydrothermal plumes (orange arrows). Depending on the efficiency of water circulation, such serpentinization fronts may induce a heat anomaly of 20-30 mW/m² in 2-6 Ma after serpentinization onset⁴⁴, increasing local geothermal gradient. Upon reaching cooler water ±HC-saturated carbonate reservoirs and superficial waters, hydrothermal venting would nucleate large quantities of silica and, if local homogenized waters achieved pH>10, spherulites and Mg-clays could precipitate. Neutralization of hyperalkaline silica-rich fluids by mixing with various proportions of acidic fluids (magmatic-hydrothermal ±CO₂ and/or meteoric) would lead to quasi-instantaneous nucleation⁴⁵ along fault planes/conducts, explaining pervasive silicification in detachment faults⁴⁶. Likewise, pH neutralization by meteoric waters during alkalinity crises of humid episodes^{8,13} illustrates an additional climatic depositional control. Common CO₂-HC fluid inclusions in hydrothermal silica cements^{16,17} and synchronicity with HC migration¹³ also suggest that serpentinization fluids and associated heat-flow may have locally influenced liquid HC synthesis/degradation.

Furthermore, it has been proposed that serpentinization of abyssal peridotites may be a “factory” of giant-salt and HC-accumulations⁴⁷. Indeed, decameter-sized carbonate-brucite chimneys/constructions are typical of serpentinite-hosted hydrothermal systems³⁷, and experimental seawater-serpentinization of peridotites precipitates anhydrite³⁰, which is often the immediate seal-rock of pre-salt carbonate HC-reservoirs. Therefore, the hydrothermal dissolution of clinopyroxenes found in peridotites and basalts could be a source of calcium for such systems. In agreement, recent thermodynamic modeling suggests that subsurface lizardite-forming serpentinization (25–250°C) generates hydrothermal brines that may be responsible for giant Aptian salt deposits of the South Atlantic⁷. This rift-serpentinization-carbonates-HC-giant salt association likely corresponds to initial stages of Wilson cycles preceding nascent oceans, which may have been recurrent during supercontinent breakups.

Finally, the South Atlantic pre-salt province may be a noteworthy analogue of Archean environments, where Lost City-type systems may have been characteristic³⁷, producing carbonates, cherts, salts, heat, hydrogen-based energy and prebiotic molecules such as methane, formate⁴⁸, carboxylic and amino acids⁴⁹. Such serpentinite-hosted hydrothermal ecosystem aggregates many favorable conditions which could have promoted the transition from inorganic carbonate constructions to organic microbial mats and stromatolites 3.5 Ga ago⁵⁰, where life on Earth and perhaps other planets may have first flourished.

Methods

The reacting material was prepared from mantle xenolith PM23, a coarse-grained spinel peridotite composed of olivine, enstatite, diopside, spinel, interstitial carbonates and trace amounts of amphibole. The peridotite was sampled at Gobernador Gregores volcanic field (Argentina), where it occurs as subspherical xenoliths (up to 60 cm in diameter) enveloped by alkali basalts. To avoid silica contamination during preparation, ceramic and plastic recipients/utensils were used whenever possible. The sample was coarsely crushed using a ceramic plates mill, manually ground with a ceramic pestle and mortar, and then dry sieved into a starting grain size of 63–180 µm, within typical range of coarse-grained fault gouges²⁶. Acid lixiviation using 0.1 M HCl during ultrasonic bath was applied to the sample to remove

supergene interstitial carbonates and very fine particles. Afterwards, the powder was rinsed several times, wet sieved with abundant deionized water and dried at 50°C for 24h. Converging X-ray fluorescence (XRF) of the dry powder and electron microprobe analyses (EMPA) of primary minerals, the starting material modal composition was determined as 76% olivine, 16% enstatite, 6% diopside and 2% spinel, hence characterized as a lherzolite-harzburgite (Table 1). The loss on ignition (LOI) of the starting peridotite powder was below 0.001 wt% (Table 1), confirming the sample is fresh and that all carbonates were successfully removed by the acid attack. Scanning electron microscopy (SEM) observations of the starting powder indicates that average particle size is closer to the upper limit (180 µm), with some grains eventually reaching 300 µm probably due to the prismatic habit of pyroxenes which may be sieved along their long axis.

Bulk LOI, major and minor elements of the starting peridotite powder were determined by XRF, while primary minerals were identified by petrographic microscope and X-ray diffraction (XRD), and their composition resolved by EMPA of thin sections (Table 1). More than 30 analyses were performed for each silicate and circa 11 analyses for spinel, all with major elements relative error below 3%, which suggests that primary minerals are homogenous. In order to assess the starting material representativity of the depleted mantle, we combined literature EMPA and mineral modes data from compilations of abyssal residual peridotites⁵¹ and serpentinites^{52,53} to estimate whole-rock average compositions of various lithotypes (Table 1). Sample PM23 closely resembles both modal and whole-rock geochemistry of average residual peridotites and, hence, it can be considered a fair analogue of the depleted upper mantle (Table 1). Finally, a seawater salinity fluid (33 g/L = 0.56 M NaCl) was prepared by adding analytical grade sodium chloride to deionized water. The solution was fully equilibrated with atmospheric carbon dioxide at room conditions and, considering an average CO_{2(atm)} concentration of 390 ppm, its dissolved concentration was estimated as 7.96 x 10⁻³ mmol/kg using the software PHREEQC-v3⁵⁴.

Experimental setup

Two sets of experiments at “low” (13.4 MPa, series Exp.A-D) and “high” (20.7 MPa, series Exp.A2-D2) pressures and constant temperature (230°C) were designed to investigate overburden effects on serpentinization kinetics. All experiments were performed at the Instituto do Petróleo e dos Recursos Naturais (IPR-PUCRS) in a non-

stirred high-pressure Hastelloy™ vessel of 75 mL capacity from Parr Instrument Company, equipped with a manometer and automatic temperature controller connected to an electric heating apparatus. The peridotite powder (14 g) and artificial saline solution (56 g) were added to achieve the initial mass ratio (W/R = 4:1), which simulates lower range estimates for serpentinization of spinel harzburgites at the Mid-Atlantic ridge⁵⁵. Only Exp.B was performed with 8 g of peridotite and 32 g of saline solution, nonetheless, maintaining equal W/R ratio. The mixture was agitated and subsequently measured for its pH_{25 °C} using a 913 Metrohm Pt1000 electrode with an uncertainty of approximately ± 0.1 units of the reported value. Remaining air in the reactor was flushed twice with argon gas pressurized up to 200 bar and successively drained to 30 bar before the headspace (ca. 15 cm³) was finally filled with pure argon gas, which guaranteed an inert reaction atmosphere. The vessel was heated at constant rate up to 230 °C and allowed to react under vapor-saturated pressures of 13.4 ± 0.8 or 20.7 ± 0.8 MPa (“low” and “high” series, respectively) in separate experimental runs for approximately 5, 14, 20 and 40 days. Experiment initiation was considered only after the target temperature was reached. During runs the temperature varied ± 5 °C mostly due to room temperature oscillation. To avoid changes in W/R ratio all samples were collected under room conditions after experiment termination. One replicate (Exp.C2R) was made of Exp.C2 in order to assure reproducibility of the results.

Post-experiment procedure

At the end of each experiment heating was turned off and the vessel naturally cooled to room temperature while still pressurized with the initial argon gas input. Quenching was not applied in order to prevent induced silica precipitation during abrupt cooling. Gas samples were taken (only in the HPS) from the pressurized vessel using a constant pressure (1 bar) sampling device coupled to the reactor valve. Samples were immediately analysed by gas chromatography (GC) using a thermal conductivity detector (TCD) for H₂ and CO₂ and a flame ionization detector (FID) for HC content. In all experiments the vessel was carefully depressurized to 1 atm using the reactor valve before it was opened, and pH_{25 °C} was immediately measured inside the reactor cup.

Fluid samples were retrieved, weighted and centrifuged at 4000 rpm for 5 min before pH_{25 °C} was measured again. Centrifuged and uncentrifuged fluid measurements always presented coherent pH values within analytical uncertainty.

Two aliquots of 5 g of the centrifuged fluid were taken from each experiment, one of which was slightly acidified with 5% HNO₃ and another kept untreated. These aliquots were diluted 10x with deionized water prior to chemical analyses using inductively coupled plasma optical emission spectroscopy (ICP-OES).

Solid products were rinsed with deionized water and centrifuged successively three times at 4000 rpm for 5 min to eliminate all saline residues, and then dried in a petri dish for 36-72 h at 40 °C. Recovered dry solids always varied +0.39-1.60 % compared to initial reactant mass, ensuring sample representativity. The powder was homogenized using a ceramic pestle and mortar, with sub-samples taken for bulk rock XRF and XRD, SEM coupled energy dispersive spectroscopy (EDS), thermogravimetric analysis (TGA) and EMP characterization. Polished epoxy-impregnated sections were used to acquire SEM images, as well as for quantitative EMPA of relict primary minerals and products.

Whole-rock X-ray Fluorescence (XRF)

Powder samples of the starting material and experimental serpentinization products were ground using a ceramic pestle and mortar to <200 mesh. The RIX 2000 (Rigaku) sequential spectrometer at Laboratório de Espectrometria por Fluorescência de raios-X (UFRGS) is equipped with a Rh X-ray tube. One gram of each sample was weighed and subsequently heated to 1000 °C for 1h to determine the loss on ignition (LOI). Samples were fused with lithium tetraborate prior to analyses. An eleven-points calibration curve was especially designed for silica-poor magnesium-rich ultramafic rocks. The standard deviation was evaluated by multiple analyses of standards, which resulted in relative errors below 0.3 % for SiO₂ and Fe₂O₃, 0.5 % for MgO and 0.9 % for other major oxides.

Whole-rock X-ray Diffraction (XRD)

X-ray diffraction of starting and reacted powders were acquired following the same sample preparation procedure described for XRF analyses. Diffraction patterns were obtained in a Siemens (Bruker-AXS) D-5000 diffractometer using Cu K- α radiation and graphite monochromator before the detector. The analysed range was 5 to 100 °2θ in a step-size of 0.02 °/15 s. Rietveld refinement of data was performed using the Maud software.

Scanning Electron Microscopy (SEM)

SEM images were obtained using a JEOL-6610LV apparatus coupled with a Quantax EDS 133 eV (Bruker) at the Laboratório de Geologia Isotópica (LGI – UFRGS) with 10-15 kV accelerating voltage. Double-sided carbon tapes sprinkled with reacted powder were double coated with gold and carbon and used for morphological evaluation of products. Supernatant fraction of the reacted material (serpentine) was obtained after 10 minutes of ultrasonic bath in absolute ethanol and pipetted onto double-sided carbon tapes and triple coated (carbon, gold, carbon) for greater beam stabilization. EDS analyses were used to investigate reacted rims and residual primary minerals both in polished epoxy-impregnated sections and carbon tapes.

Electron Microprobe Analyses (EMPA)

EMPA were carried out using a Cameca SXFive installed at the Laboratório de Microssonda Eletrônica (UFRGS). Operating conditions for starting peridotite thin sections were accelerating potential of 15 keV, 15 nA current and 5 µm beam size for all minerals. After experimental runs, relict olivine, pyroxenes and spinel were analysed using the same parameters, while serpentine was analysed with 15 keV accelerating potential, 6-20 nA current and 5-10 µm beam size to avoid devolatilization. Quantitative element distribution maps were obtained using 15 keV accelerating potential, 100 nA current and 5 µm beam size.

Thermogravimetric analyses (TGA)

Analyses for all serpentized samples and the reactant peridotite were performed with a Shimadzu TGA-50 instrument at the Laboratório de Altas Pressões e Materiais Avançados (LAPMA - UFRGS) under the following conditions: sample mass of ~15 mg, platinum crucible with a pinhole, heating rate of 10 °C.min⁻¹ up to 900 °C (up to 1000°C only for the protolith and Exp.A2) and inert argon or nitrogen atmosphere using a 50 ml.min⁻¹ flow rate. Sample mass loss was obtained by TGA and, in order to identify the different mass loss steps, the first derivative was used. The TGA apparatus was calibrated in terms of temperature and background correction for results were applied using runs made with an empty crucible as reference. Background

subtraction and mass loss interval interpretation were performed using the TA-60WS software package. The mass loss was less than 0.01 mg comparing empty crucible against empty crucible, i.e. equal to the limit of experimental error.

Inductively coupled plasma optical emission spectrometry (ICP-OES) analyses

The aqueous samples were filtered in Polyvinylidene Fluoride (PVDF) 0.22 µm membranes, diluted with 5% HNO₃ and analysed using inductively coupled plasma optical emission spectrometry (Perkin Elmer Optima 7000 DV) at IPR-PUCRS. The calibration curve for Al, Ca, Cr, Fe, Mg, Mn and Ni was constructed using standard concentrations of 2.5, 5, 10, 50, 100, 200, 500 and 1000 µg.L⁻¹ with a multi-elemental calibration solution, and dilutions were performed with deionized water (18.2 MΩ·cm). The correlation coefficient of the analytical curve was greater than or equal to 0.999. Silicon concentration was independently determined using a silicon mono-elemental calibration solution, by diluting sub-samples with either 5% HNO₃ or only pure deionized water, always reaching similar results within analytical error. A silicon calibration curve was also constructed using standard concentrations of 2.5, 5, 10, 50, 100, 200, 500 and 1000 µg.L⁻¹, and the analysis followed typical procedure used for metal determination in multi-element standard solutions.

Gas chromatography (GC) and Ionic chromatography (IC)

Determination of CO₂, CH₄, and H₂ concentration was performed by gas chromatography on GC-2014 (Shimadzu) using helium as a carrier gas with a flow rate of 38.5 mL.min⁻¹. The chromatograph is equipped with a flame ionization detector (FID) connected with a Carboxen Plot 1006 capillary column, which is used to quantify CH₄ and CO₂, and a thermal conductivity detector (TCD) linked to two Hayesep columns and one 5 angstroms molecular sieve column, used in the determination of H₂. Injector and detector temperatures were adjusted to 150 °C and 307 °C, respectively. The GC oven temperature was initially set at 40 °C (maintained for 4 min.) and then heated at a rate of 14 °C.min⁻¹ to 180 °C (maintained for 1 min.). Analysis of Cl in solution was performed on an ICS-5000 ion chromatograph equipped with a dual pump module and eluent generation module. The eluent used for the determination of anions was potassium hydroxide (KOH), in a concentration gradient ranging from 5 mM to 35 mM

and flow rate of 0.250 mL·min⁻¹. The detection mode used was conductivity, together with suppressor model ASRS 300 2 mm. A calibration curve was constructed using ThermoFisher Scientific multi-anion standard Dionex Combined Seven Anions Standard II. The calibration curve was constructed with 7 points ranging from 1 to 100 mg·L⁻¹ for chloride, resulting in a correlation coefficient equal to or greater than 99.8%.

References

1. Foulger, G. R. Origin of the South Atlantic igneous province. *J. Volcanol. Geotherm. Res.* **355**, 2–20 (2018).
2. Alves, S. et al. Characterization of subaerial volcanic facies using acoustic image logs : Lithofacies and log-facies of a lava-flow deposit in the Brazilian pre-salt , deepwater of Santos Basin. *Mar. Pet. Geol.* **99**, 156–174 (2019).
3. Alvarenga, R. S., Iacopini, D., Kuchle, J., Scherer, C. M. S. & Goldberg, K. Seismic characteristics and distribution of hydrothermal vent complexes in the Cretaceous offshore rift section of the Campos Basin, offshore Brazil. *Mar. Pet. Geol.* **74**, 12–25 (2016).
4. Neto, E. V. S., Cerqueira, J. R. & Prinzhofer, A. Origin of CO₂ in Brazilian Basins. *AAPG Annu. Conv. Exhib.* **40969**, (2012).
5. Zalán, P. V et al. An Entirely New 3D-View of the Crustal and Mantle Structure of a South Atlantic Passive Margin – Santos , Campos and Espírito Santo Basins , Brazil. in *AAPG Annual Conference and Exhibition* (2011).
6. Dias, J. L. Tectônica, estratigrafia e sedimentação no Andar Aptiano da margem leste brasileira. *Bol. Geociências da Petrobras* **13**, 7–25 (2004).
7. Debure, M. et al. Thermodynamic evidence of giant salt deposit formation by serpentinization: an alternative mechanism to solar evaporation. *Sci. Rep.* **9**, 1–11 (2019).
8. Wright, V. P. & Barnett, A. J. An abiotic model for the development of textures in some South Atlantic early Cretaceous lacustrine carbonates. *Geol. Soc. London, Spec. Publ.* **418**, 209–219 (2015).
9. Tutolo, B. M. & Tosca, N. J. Experimental examination of the Mg-silicate-

- carbonate system at ambient temperature: Implications for alkaline chemical sedimentation and lacustrine carbonate formation. *Geochim. Cosmochim. Acta* **225**, 80–101 (2018).
10. Saller, A. *et al.* Presalt stratigraphy and depositional systems in the Kwanza Basin, offshore Angola. *Am. Assoc. Pet. Geol. Bull.* **100**, 1135–1164 (2016).
 11. Wright, V. P. Lacustrine carbonates in rift settings: the interaction of volcanic and microbial processes on carbonate deposition. *Geol. Soc. London, Spec. Publ.* **370**, 39–47 (2012).
 12. Herlinger, R., Zambonato, E. E. & De Ros, L. F. Influence of Diagenesis On the Quality of Lower Cretaceous Pre-salt Lacustrine Carbonate Reservoirs from Northern Campos Basin, Offshore Brazil. *J. Sediment. Res.* **87**, 1285–1313 (2017).
 13. Tritlla, J. *et al.* Carbonates That Are No More: Silicified Pre-Salt Oil Reservoirs in Campos Basin (Brazil). *AAPG ACE 2018 Abstr.* (2018).
 14. Teboul, P. A. *et al.* Diversity and origin of quartz cements in continental carbonates: Example from the Lower Cretaceous rift deposits of the South Atlantic margin. *Appl. Geochemistry* **100**, 22–41 (2019).
 15. Teboul, P.-A. *et al.* Volcanic rock alterations of the Kwanza Basin, offshore Angola - Insights from an integrated petrological, geochemical and numerical approach. *Mar. Pet. Geol.* **80**, 394–411 (2017).
 16. Girard, J.-P. & Miguel, G. S. Hydrothermal Diagenesis and Reservoir Quality in the Pre-Salt Carbonate-Clastic Series of the Kwanza Basin , Offshore Angola. in *AAPG ACE 2018 Annual Convention & Exhibition* (2018).
 17. Poros, Z. *et al.* Origin of Silica in Pre-Salt Carbonates , Kwanza Basin , Angola. *AAPG Annu. Conf. Exhib.* **51413**, 3200 (2017).
 18. Szatmari, P. & Milani, E. J. Tectonic control of the oil-rich large igneous-carbonate-salt province of the South Atlantic rift. *Mar. Pet. Geol.* (2016). doi:10.1016/j.marpetgeo.2016.06.004

19. Rogerson, M. *et al.* Are spherulitic lacustrine carbonates an expression of large-scale mineral carbonation? A case study from the East Kirkton Limestone, Scotland. *Gondwana Res.* **48**, 101–109 (2017).
20. Pinto, V. H. G., Manatschal, G., Karpoff, A. M., Ulrich, M. & Viana, A. R. Seawater storage and element transfer associated with mantle serpentinization in magma-poor rifted margins: A quantitative approach. *Earth Planet. Sci. Lett.* **459**, 227–237 (2017).
21. Andreani, M., Grauby, O., Baronnet, A. & Muñoz, M. Occurrence, composition and growth of polyhedral serpentine. *Eur. J. Mineral.* **20**, 159–171 (2008).
22. Toft, P. B., Arkani-Hamed, J. & Haggerty, S. E. The effects of serpentinization on density and magnetic susceptibility: a petrophysical model. *Phys. Earth Planet. Inter.* **65**, 137–157 (1990).
23. Oufi, O., Cannat, M. & Horen, H. Magnetic properties of variably serpentized abyssal peridotites. *J. Geophys. Res.* **107**, (2002).
24. Bach, W. *et al.* Unraveling the sequence of serpentinization reactions: Petrography, mineral chemistry, and petrophysics of serpentinites from MAR 15°N (ODP Leg 209, Site 1274). *Geophys. Res. Lett.* **33**, (2006).
25. Gunnarsson, I. & Arnórsson, S. Amorphous silica solubility and the thermodynamic properties of H_4SiO_4 in the range of 0° to 350°C at Psat. *Geochim. Cosmochim. Acta* **64**, 2295–2307 (2000).
26. Wang, G., Mitchell, T. M., Meredith, P. G., Nara, Y. & Wu, Z. Influence of gouge thickness and grain size on permeability of macrofractured basalt. *J. Geophys. Res. Solid Earth* **121**, 8472–8487 (2016).
27. Marcaillou, C., Muñoz, M., Vidal, O., Parra, T. & Harfouche, M. Mineralogical evidence for H₂ degassing during serpentinization at 300°C/300bar. *Earth Planet. Sci. Lett.* **303**, 281–290 (2011).
28. Huang, R. *et al.* Influence of pyroxene and spinel on the kinetics of peridotite serpentinization. *J. Geophys. Res. Solid Earth* **122**, 7111–7126 (2017).
29. Evans, B. W. The Serpentinite Multisystem Revisited: Chrysotile Is Metastable. *Int. Geol. Rev.* **46**, 479–506 (2004).

30. Seyfried, W. E., Foustoukos, D. I. & Fu, Q. Redox evolution and mass transfer during serpentinization: An experimental and theoretical study at 200°C, 500 bar with implications for ultramafic-hosted hydrothermal systems at Mid-Ocean Ridges. *Geochim. Cosmochim. Acta* **71**, 3872–3886 (2007).
31. Klein, F., Bach, W. & McCollom, T. M. Compositional controls on hydrogen generation during serpentinization of ultramafic rocks. *Lithos* (2013). doi:10.1016/j.lithos.2013.03.008
32. Mellini, M. The crystal structure of lizardite 1T: hydrogen bonds and polytypism. *Am. Mineral.* **67**, 587–598 (1982).
33. Andreani, M., Muñoz, M., Marcaillou, C. & Delacour, A. μ XANES study of iron redox state in serpentine during oceanic serpentinization. *Lithos* **178**, 70–83 (2013).
34. Frost, B. R. & Beard, J. S. On Silica Activity and Serpentinization. *J. Petrol.* **48**, 1351–1368 (2007).
35. Mayhew, L. E., Ellison, E. T., McCollom, T. M., Trainor, T. P. & Templeton, A. S. Hydrogen generation from low-temperature water–rock reactions. *Nat. Geosci.* **6**, 478–484 (2013).
36. Etiope, G. & Sherwood Lollar, B. Abiotic methane on earth. *Rev. Geophys.* **51**, 276–299 (2013).
37. Kelley, D. S. *et al.* A serpentinite-hosted ecosystem: the Lost City hydrothermal field. *Science (80-.).* **307**, 1428–34 (2005).
38. Seyfried, W. E., Pester, N. J., Tutolo, B. M. & Ding, K. The Lost City hydrothermal system: Constraints imposed by vent fluid chemistry and reaction path models on subseafloor heat and mass transfer processes. *Geochim. Cosmochim. Acta* **163**, 59–79 (2015).
39. Allen, D. E. & Seyfried, W. E. Serpentinization and heat generation: Constraints from Lost City and Rainbow hydrothermal systems. *Geochim. Cosmochim. Acta* **68**, 1347–1354 (2004).

40. Katayama, I., Kurosaki, I. & Hirauchi, K. Low silica activity for hydrogen generation during serpentinization: An example of natural serpentinites in the Mineoka ophiolite complex, central Japan. *Earth Planet. Sci. Lett.* **298**, 199–204 (2010).
41. Tobler, D. J. & Benning, L. G. In situ and time resolved nucleation and growth of silica nanoparticles forming under simulated geothermal conditions. *Geochim. Cosmochim. Acta* **114**, 156–168 (2013).
42. McCollom, T. M. *et al.* Temperature trends for reaction rates, hydrogen generation, and partitioning of iron during experimental serpentinization of olivine. *Geochim. Cosmochim. Acta* **181**, 175–200 (2016).
43. Lee, H. *et al.* Massive and prolonged deep carbon emissions associated with continental rifting. *Nat. Geosci.* **9**, 145–149 (2016).
44. Delescluse, M. & Chamot-rooke, N. Serpentinization pulse in the actively deforming Central Indian Basin. *Earth Planet. Sci. Lett.* **276**, 140–151 (2008).
45. Tobler, D. J., Shaw, S. & Benning, L. G. Quantification of initial steps of nucleation and growth of silica nanoparticles: An in-situ SAXS and DLS study. *Geochim. Cosmochim. Acta* **73**, 5377–5393 (2009).
46. Bonnemains, D., Escartín, J., Mével, C., Andreani, M. & Verlaguet, A. Pervasive silicification and hanging wall overplating along the 13°20'N oceanic detachment fault (Mid-Atlantic Ridge). *Geochemistry, Geophys. Geosystems* **18**, 2028–2053 (2017).
47. Manuella, F. C., Scribano, V. & Carbone, S. Abyssal serpentinites as gigantic factories of marine salts and oil. *Mar. Pet. Geol.* **92**, 1041–1055 (2018).
48. Lang, S. Q. *et al.* Deeply-sourced formate fuels sulfate reducers but not methanogens at Lost City hydrothermal field. *Sci. Rep.* **8**, 1–10 (2018).
49. Ménez, B. *et al.* Abiotic synthesis of amino acids in the recesses of the oceanic lithosphere. *Nature* **564**, 59–63 (2018).
50. Baumgartner, R. J. *et al.* Nano-porous pyrite and organic matter in 3.5-billion-year-old stromatolites record primordial life. *Geology* **47**, 1–5 (2019).
51. Warren, J. M. Global variations in abyssal peridotite compositions. *Lithos* **248–251**, 193–219 (2016).

52. Deschamps, F., Godard, M., Guillot, S. & Hattori, K. Geochemistry of subduction zone serpentinites: A review. *Lithos* **178**, 96–127 (2013).
53. Peters, D., Bretscher, A., John, T., Scambelluri, M. & Pettke, T. Fluid-mobile elements in serpentinites: Constraints on serpentinisation environments and element cycling in subduction zones. *Chem. Geol.* **466**, 654–666 (2017).
54. Parkhurst, D. L. & Appelo, C. A. J. Description of input and examples for PHREEQC version 3 - A computer program for speciation, batch-reaction, one-dimensional transport, and inverse geochemical calculations. in *U.S. Geological Survey Techniques and Methods* (USGS, 2013).
55. Vils, F., Tonarini, S., Kalt, A. & Seitz, H. M. Boron, lithium and strontium isotopes as tracers of seawater-serpentinite interaction at Mid-Atlantic ridge, ODP Leg 209. *Earth Planet. Sci. Lett.* **286**, 414–425 (2009).

CAPÍTULO III – COMPLEMENTOS E ANEXOS

ANEXO A - Tabela 1. EMP data of primary minerals from peridotite mantle xenolith PM23.

Olivine (n= 30)											
wt%	Mean	Median	σ	Min.	Max.	apfu	Mean	Median	σ	Min.	Max.
Na ₂ O	0.01	0.01	0.01	0.00	0.02	Na	0.00	0.00	0.000	0.00	0.00
SiO ₂	41.34	41.36	0.19	40.95	41.65	Si	1.01	1.01	0.002	1.00	1.01
MgO	49.06	49.07	0.25	48.43	49.52	Mg	1.79	1.78	0.004	1.78	1.79
Al ₂ O ₃	0.00	0.00	0.00	0.00	0.01	Al	0.00	0.00	0.000	0.00	0.00
K ₂ O	0.00	0.00	0.01	0.00	0.02	K	0.00	0.00	0.000	0.00	0.00
CaO	0.03	0.03	0.02	0.00	0.07	Ca	0.00	0.00	0.001	0.00	0.00
FeO	8.90	8.89	0.07	8.72	9.01	Fe	0.18	0.18	0.001	0.18	0.19
TiO ₂	0.01	0.00	0.01	0.00	0.05	Ti	0.00	0.00	0.000	0.00	0.00
Cr ₂ O ₃	0.04	0.03	0.03	0.00	0.12	Cr	0.00	0.00	0.001	0.00	0.00
MnO	0.12	0.12	0.02	0.08	0.19	Mn	0.00	0.00	0.001	0.00	0.00
V ₂ O ₃	0.01	0.00	0.01	0.00	0.05	V	0.00	0.00	0.000	0.00	0.00
CoO	0.01	0.01	0.01	0.00	0.04	Co	0.00	0.00	0.000	0.00	0.00
NiO	0.39	0.40	0.03	0.32	0.47	Ni	0.01	0.01	0.001	0.01	0.01
Ga ₂ O ₃	0.03	0.01	0.04	0.00	0.15	Ga	0.00	0.00	0.001	0.00	0.00
Ce ₂ O ₃	0.03	0.01	0.03	0.00	0.10	Ce	0.00	0.00	0.000	0.00	0.00
Total	99.99	100.05	0.44	98.94	100.62	Total	2.99	2.99	0.002	2.99	3.00
						Mg#	90.76	90.76	0.08	90.59	90.89
						Mg/Si	1.77	1.77	0.01	1.76	1.79
						Ni/Cr	7.00	8.00	1.75	4.00	9.00
						Al/Si	0.00	0.00	0.00	0.00	0.00
						Σ cations+3	0.00	0.00			

Enstatite (n= 30)											
wt%	Mean	Median	σ	Min.	Max.	apfu	Mean	Median	σ	Min.	Max.
Na ₂ O	0.09	0.09	0.01	0.07	0.13	Na	0.01	0.01	0.001	0.00	0.01
SiO ₂	56.23	56.28	0.28	55.71	56.79	Si	1.93	1.93	0.007	1.92	1.95
MgO	33.16	33.14	0.20	32.83	33.81	Mg	1.70	1.70	0.007	1.69	1.72
Al ₂ O ₃	3.52	3.46	0.26	3.21	4.12	Al	0.14	0.14	0.010	0.13	0.17
K ₂ O	0.00	0.00	0.01	0.00	0.03	K	0.00	0.00	0.000	0.00	0.00
CaO	0.51	0.50	0.07	0.45	0.83	Ca	0.02	0.02	0.002	0.02	0.03
FeO	5.67	5.66	0.08	5.49	5.78	Fe	0.16	0.16	0.002	0.16	0.17
TiO ₂	0.10	0.11	0.02	0.06	0.14	Ti	0.00	0.00	0.001	0.00	0.00
Cr ₂ O ₃	0.49	0.49	0.07	0.40	0.68	Cr	0.01	0.01	0.002	0.01	0.02
MnO	0.13	0.13	0.03	0.05	0.17	Mn	0.00	0.00	0.001	0.00	0.01
V ₂ O ₃	0.02	0.02	0.02	0.00	0.05	V	0.00	0.00	0.001	0.00	0.00
CoO	0.01	0.00	0.01	0.00	0.04	Co	0.00	0.00	0.000	0.00	0.00
NiO	0.09	0.09	0.02	0.04	0.15	Ni	0.00	0.00	0.001	0.00	0.00
Ga ₂ O ₃	0.03	0.02	0.03	0.00	0.14	Ga	0.00	0.00	0.001	0.00	0.00
Ce ₂ O ₃	0.02	0.01	0.02	0.00	0.08	Ce	0.00	0.00	0.000	0.00	0.00
Total	100.06	100.12	0.41	99.18	101.02	Total	3.99	3.99	0.003	3.98	4.00
						Mg#	91.26	91.26	0.11	91.04	91.51
						Mg/Si	0.88	0.88	0.00	0.87	0.89
						Ni/Cr	0.20	0.18	0.06	0.07	0.31
						Al/Si	0.07	0.07	0.01	0.07	0.09
						Σ cations+3	0.16	0.15			

Diopside (n= 30)											
wt%	Mean	Median	σ	Min.	Max.	apfu	Mean	Median	σ	Min.	Max.
Na ₂ O	1.99	1.99	0.04	1.89	2.06	Na	0.14	0.14	0.003	0.13	0.15
SiO ₂	52.63	52.62	0.28	52.09	53.33	Si	1.91	1.91	0.006	1.90	1.92
MgO	14.53	14.50	0.14	14.29	14.88	Mg	0.79	0.79	0.006	0.78	0.80
Al ₂ O ₃	5.95	5.95	0.15	5.64	6.20	Al	0.25	0.26	0.007	0.24	0.27
K ₂ O	0.00	0.00	0.01	0.00	0.02	K	0.00	0.00	0.000	0.00	0.00
CaO	20.20	20.26	0.13	19.93	20.37	Ca	0.79	0.79	0.006	0.77	0.79
FeO	2.14	2.14	0.06	2.00	2.25	Fe	0.06	0.07	0.002	0.06	0.07
TiO ₂	0.54	0.54	0.05	0.46	0.64	Ti	0.01	0.01	0.001	0.01	0.02
Cr ₂ O ₃	1.37	1.39	0.12	1.13	1.54	Cr	0.04	0.04	0.003	0.03	0.04
MnO	0.07	0.07	0.02	0.03	0.12	Mn	0.00	0.00	0.001	0.00	0.00
V ₂ O ₃	0.05	0.04	0.02	0.01	0.08	V	0.00	0.00	0.001	0.00	0.00
CoO	0.01	0.00	0.01	0.00	0.05	Co	0.00	0.00	0.000	0.00	0.00
NiO	0.03	0.03	0.03	0.00	0.09	Ni	0.00	0.00	0.001	0.00	0.00
Ga ₂ O ₃	0.02	0.00	0.02	0.00	0.08	Ga	0.00	0.00	0.001	0.00	0.00
Ce ₂ O ₃	0.00	0.00	0.01	0.00	0.05	Ce	0.00	0.00	0.000	0.00	0.00
Total	99.53	99.51	0.33	99.01	100.39	Total	4.00	4.00	0.003	3.99	4.00
						Mg#	92.38	92.37	0.18	92.05	92.75
						Mg/Si	0.41	0.41	0.00	0.41	0.42
						Ni/Cr	0.02	0.02	0.03	0.00	0.07
						Al/Si	0.13	0.13	0.00	0.13	0.14
						Σ cations+3	0.29	0.30			

Spinel (n= 11)											
wt%	Mean	Median	σ	Min.	Max.	apfu	Mean	Median	σ	Min.	Max.
SiO ₂	0.03	0.03	0.02	0.00	0.06	Si	0.00	0.00	0.000	0.00	0.00
MgO	19.99	19.98	0.14	19.82	20.24	Mg	0.79	0.79	0.005	0.78	0.80
Al ₂ O ₃	51.02	50.94	0.26	50.64	51.50	Al	1.60	1.60	0.006	1.59	1.60
CaO	0.01	0.00	0.01	0.00	0.02	Ca	0.00	0.00	0.000	0.00	0.00
FeO	10.69	10.68	0.08	10.56	10.81	Fe	0.24	0.24	0.002	0.23	0.24
Cr ₂ O ₃	17.61	17.55	0.23	17.30	17.98	Cr	0.37	0.37	0.005	0.36	0.38
MnO	0.12	0.13	0.02	0.08	0.16	Mn	0.00	0.00	0.001	0.00	0.00
TiO ₂	0.17	0.17	0.03	0.12	0.22	Ti	0.00	0.00	0.001	0.00	0.00
ZnO	0.10	0.12	0.04	0.04	0.14	Zn	0.00	0.00	0.001	0.00	0.00
V ₂ O ₃	0.07	0.07	0.02	0.03	0.10	V	0.00	0.00	0.000	0.00	0.00
NiO	0.32	0.32	0.03	0.28	0.36	Ni	0.01	0.01	0.001	0.01	0.01
CoO	0.02	0.02	0.02	0.00	0.05	Co	0.00	0.00	0.000	0.00	0.00
Ga ₂ O ₃	0.03	0.00	0.04	0.00	0.11	Ga	0.00	0.00	0.001	0.00	0.00
Ce ₂ O ₃	0.01	0.00	0.01	0.00	0.04	Ce	0.00	0.00	0.000	0.00	0.00
Total	100.19	100.23	0.26	99.75	100.55	Total	3.01	3.01	0.002	3.01	3.02
						Mg#	76.93	76.95	0.18	76.67	77.21
						Cr#	18.79	18.76	0.19	18.60	19.16

Olivine and Spinel based on 4 Oxigens; Pyroxens based on 6 Oxigens; Mg# = (Mg/Mg+Fe)*100; Cr# = (Cr/Cr+Al)*100

ANEXO A - Tabela 1. Normalized whole-rock XRF and mineral mode of sample PM23 compared to residual abyssal peridotites and serpentinites from literature.

PERIODOTITES	This study	modified after Warren 2016												Average Mineral Mode						
	PM23	1. All Peridotites (n= 162)			2. Harzburgites (n= 116/162)			3. Lherzolites (n= 45/162)			Olivine	PM23	1	2	3					
	Mean	Mean	Median	σ	Mean	Median	σ	Mean	Median	σ		76	74	76	70					
SiO ₂	43.43	43.70	43.78	0.97	43.55	43.57	0.98	44.04	44.02	0.88	Opx	16	21	21	22					
TiO ₂	0.07	0.02	0.01	0.02	0.01	0.01	0.01	0.03	0.03	0.02	Cpx	6	4	2	7					
Al ₂ O ₃	1.92	1.48	1.42	0.67	1.27	1.26	0.57	1.98	1.96	0.54	Spinel	2	1	1	1					
Cr ₂ O ₃	0.38	0.40	0.38	0.17	0.42	0.40	0.19	0.36	0.35	0.10	Total	100	100	100	100					
Fe ₂ O ₃	8.28	8.26	8.24	0.38	8.23	8.22	0.41	8.32	8.34	0.31										
MnO	0.11	0.13	0.13	0.02	0.13	0.13	0.02	0.13	0.13	0.02	Spinel Mg#	77	72	71	75					
NiO	0.30	0.26	0.27	0.05	0.27	0.28	0.05	0.25	0.25	0.04	Spinel Cr#	19	29	33	19					
MgO	44.01	44.57	44.79	1.93	45.24	45.13	1.62	42.98	43.07	1.51										
CaO	1.51	1.16	1.12	0.62	0.87	0.86	0.40	1.85	1.79	0.40										
Na ₂ O	b.d.	0.02	0.01	0.03	0.01	0.01	0.01	0.05	0.04	0.04										
K ₂ O	b.d.	n.a.	n.a.	n.a.	n.a.	n.a.	n.a.	n.a.	n.a.	n.a.										
P ₂ O ₅	b.d.	n.a.	n.a.	n.a.	n.a.	n.a.	n.a.	n.a.	n.a.	n.a.										
LOI	0.00	0.00	0.00	0.00	0.00	0.00	0.00	0.00	0.00	0.00										
Total	100.00	100.00	100.00		100.00	100.00		100.00	100.00											
SERPENTINITES	modified after Deschamps et al. 2013												modified after Peters et al. 2017							
	4. All Serpentinites* (n= 372)			5. All Serpentinites Lzd (n= 290/372)			6. Abyssal Serpentinites Lzd (n= 37/372)			7. Harzburgite-derived Serpentinites (n= 284/372)			8. Lherzolite-derived Serpentinites** (n= 20/372)			9. MOR Serpentinites (n= 128)				
	Mean	Median	σ	Mean	Median	σ	Mean	Median	σ	Mean	Median	σ	Mean	Median	σ	Mean	Median	σ		
SiO ₂	38.84	38.91	2.22	38.63	38.60	1.95	39.03	38.44	2.12	38.88	38.91	2.04	39.28	38.98	2.57	38.63	38.45	2.14		
TiO ₂	0.04	0.01	0.14	0.03	0.01	0.12	0.01	0.01	0.00	0.03	0.01	0.11	0.12	0.06	0.22	0.02	0.02	0.02		
Al ₂ O ₃	1.41	0.69	2.28	1.02	0.61	1.56	0.56	0.58	0.14	1.26	0.71	1.70	3.11	2.23	3.57	0.76	0.64	0.47		
Cr ₂ O ₃	0.37	0.34	0.11	0.37	0.34	0.11	0.33	0.35	0.10	0.36	0.33	0.11	n.d.	n.d.	n.d.	n.a.	n.a.	n.a.		
Fe ₂ O ₃	7.65	7.49	1.12	7.57	7.45	0.94	7.16	7.20	0.58	7.63	7.49	0.99	7.72	7.59	1.35	8.20	7.60	1.93		
MnO	0.13	0.10	0.51	0.11	0.10	0.03	0.09	0.09	0.02	0.14	0.10	0.58	0.13	0.12	0.05	0.10	0.10	0.04		
NiO	0.28	0.28	0.03	0.28	0.28	0.03	0.28	0.28	0.02	0.28	0.28	0.01	n.d.	n.d.	n.d.	n.a.	n.a.	n.a.		
MgO	38.23	38.56	3.57	38.70	39.43	3.62	39.40	39.64	0.91	38.60	39.10	2.96	34.45	36.36	6.97	38.43	38.67	2.16		
CaO	0.72	0.38	1.24	0.73	0.42	1.31	0.17	0.07	0.18	0.56	0.36	1.00	2.65	2.23	2.30	0.64	0.27	1.01		
Na ₂ O	0.12	0.06	0.32	0.12	0.06	0.32	0.09	0.11	0.05	0.08	0.05	0.21	0.49	0.05	1.15	0.14	0.11	0.13		
K ₂ O	0.02	0.02	0.05	0.02	0.02	0.05	0.01	0.01	0.01	0.02	0.02	0.21	0.04	0.31	0.02	0.02	0.02	0.02		
P ₂ O ₅	0.02	0.01	0.06	0.02	0.01	0.06	0.01	0.01	0.00	0.01	0.01	0.03	0.09	0.01	0.23	0.03	0.02	0.03		
LOI	12.86	12.79	1.35	13.06	13.10	1.37	13.38	13.13	1.11	12.80	12.72	1.24	12.24	12.04	1.65	13.17	13.17	1.18		
Total	100.00	100.00		100.00	100.00		100.00	100.00		100.00	100.00		100.00	100.00		100.00	100.00			
DELTA SERPENTINIZATION	$\Delta\%$ (4:1)				$\Delta\%$ (5:1)				$\Delta\%$ (6:1)				$\Delta\%$ (9:1)				$\Delta\%$ (4:2)			
	Mean	Median	Mean	Median	Mean	Median	Mean	Median	Mean	Median	Mean	Median	Mean	Median	Median	Mean	Median	Mean	$\Delta\%$ (7:2)	$\Delta\%$ (9:2)
	-11.11	-11.12	-11.59	-11.83	-10.69	-12.21	-11.60	-12.18	-10.81	-10.70	-11.30	-11.42	-10.40	-11.79	-10.73	-10.70	-11.31	-11.77		
SiO ₂	-115.20	-27.58	62.25	-40.42	-56.80	-43.63	11.64	1.07	207.18	-15.03	131.59	-30.09	-38.33	-33.86	132.74	-20.05	59.35	18.58		
TiO ₂	-4.71	-51.76	-31.11	-56.94	-61.94	-59.09	-48.89	-55.40	11.20	-45.70	-19.61	-51.52	-55.59	-53.95	-0.97	-43.52	-40.35	-49.79		
Al ₂ O ₃	-8.50	-9.69	-8.50	-9.69	-17.07	-8.86	n.a.	n.a.	-11.74	-13.56	-11.74	-13.56	-20.01	-12.77	-14.21	-17.56	n.a.	n.a.		
Cr ₂ O ₃	-7.33	-9.07	-8.36	-9.59	-13.33	-12.70	-0.76	-7.81	-7.06	-8.87	-8.09	-9.39	-13.08	-12.50	-7.28	-8.95	-0.47	-7.60		
MnO	3.52	-19.00	-17.92	-19.15	-31.89	-30.48	-20.38	-22.57	4.60	-18.80	-17.06	-18.95	-31.18	-30.30	9.46	-18.79	-19.55	-22.38		
NiO	6.41	5.15	6.41	5.15	6.27	5.14	n.a.	n.a.	4.66	2.32	4.66	2.32	4.52	2.31	4.77	2.24	n.a.	n.a.		

Serpentinites selection criterion: Oxide sum pre-normalization 95-101.9 wt%, LOI 10-16 wt%, Modal serpentine >70%; Fe_2O_3 as total iron; *Abyssal, mantle edge and subduction serpentinites (Lzd & Atg); **All subduction related; $\Delta\%$ (X:Y) = Delta oxide Serpentinite X versus Peridotite Y; b.d. = below detection, n.a. = not available, LOI = Loss on ignition, Mg# = $(\text{Mg}/(\text{Mg}+\text{Fe})) \times 100$, Cr# = $(\text{Cr}/(\text{Cr}+\text{Al})) \times 100$, Lzd = mainly lizardite, Atg = mainly antigorite; Delta for K_2O and P_2O_5 n.a.

ANEXO B - Tabela 2: Olivine-derived serpentine EMPA from both experimental pressures sets.

Run	DataSet	Nb of Ions																		Total	Mg/Si	Ni/Cr	Al/Si	Σcations t.o.c.	Σcations+3	Mg#	Fe ⁺³ / Fe total	% Charge balance*												
		SiO ₂	MgO	FeO	Al ₂ O ₃	NiO	Cr ₂ O ₃	MnO	CaO	TiO ₂	V ₂ O ₃	CoO	Ga ₂ O ₃	Ce ₂ O ₃	Na ₂ O	Cl	Total	Mg	Fe	Al	Ni	Cr	Mn	Ca	Ti	V	Co	Ga	Ce	Na	Cl	OH								
High Pressure Series (20.7 MPa / 230°C)																																								
Exp. A2 (N = 13)	Mean	35.83	35.84	6.55	1.02	0.44	0.05	0.09	0.04	0.01	n.a.	0.00	n.a.	n.a.	0.02	0.25	80.13	1.89	2.82	0.29	0.06	0.02	0.00	0.00	0.00	n.a.	0.00	0.02	3.98	9.09	1.49	22.82	0.03	5.09	3.08	0.111	92.15	16.82	+0.05	(Mg _{0.82} , Fe ⁺² _{0.24} , Ni _{0.02})(Si _{1.89} , Al _{0.06} , Fe ⁺³ _{0.05})O ₃ (OH _{3.98} , Cl _{0.02})
	Median	35.54	35.18	6.57	1.11	0.43	0.03	0.10	0.03	0.00	n.a.	0.00	n.a.	n.a.	0.02	0.23	79.65	1.89	2.79	0.28	0.07	0.02	0.00	0.00	0.00	n.a.	0.00	0.02	3.98	9.08	1.46	10.67	0.04	5.08	3.05	0.110	92.14	15.68	0.00	(Mg _{0.79} , Fe ⁺² _{0.24} , Ni _{0.02})(Si _{1.89} , Al _{0.07} , Fe ⁺³ _{0.04})O ₃ (OH _{3.98} , Cl _{0.02})
	σ	0.91	2.28	0.82	0.62	0.08	0.06	0.02	0.01	0.01	n.a.	0.00	n.a.	n.a.	0.01	0.10	31.8	0.05	0.10	0.03	0.04	0.00	0.00	0.00	0.00	n.a.	0.00	0.01	0.05	28.24	0.02	0.05								
	Min.	34.50	33.73	4.95	0.10	0.35	0.00	0.05	0.01	0.00	n.a.	0.00	n.a.	n.a.	0.00	0.12	75.51	1.78	2.74	0.23	0.01	0.01	0.00	0.00	0.00	n.a.	0.00	0.01	3.96	9.02	1.37	2.58	0.00	5.02						
	Max.	37.71	41.11	7.79	1.96	0.57	0.21	0.11	0.06	0.04	n.a.	0.00	n.a.	n.a.	0.04	0.43	85.05	2.00	3.10	0.35	0.12	0.02	0.01	0.00	0.00	n.a.	0.00	0.04	3.99	9.23	1.75	93.00	0.06	5.23						
Exp. B2 (N = 24)	Mean	38.45	34.07	6.66	1.37	0.41	0.03	0.10	0.05	0.02	n.a.	0.00	n.a.	n.a.	0.02	0.19	81.36	1.98	2.61	0.29	0.08	0.02	0.00	0.00	0.00	n.a.	0.00	0.02	3.98	8.99	1.33	16.64	0.04	4.99	2.98	0.088	90.29	1.93	0.00	(Mg _{0.61} , Fe ⁺² _{0.24} , Al _{0.06} , Ni _{0.02} , Fe ⁺³ _{0.01})(Si _{1.89} , Al _{0.09})O ₃ (OH _{3.98} , Cl _{0.02})
	Median	38.41	32.82	6.61	1.56	0.39	0.01	0.10	0.05	0.01	n.a.	0.00	n.a.	n.a.	0.02	0.16	80.99	1.99	2.54	0.28	0.10	0.02	0.00	0.00	0.00	n.a.	0.00	0.01	3.99	8.96	1.28	12.20	0.05	4.96	2.93	0.180	92.68	29.01	0.00	(Mg _{0.79} , Fe ⁺² _{0.24} , Ni _{0.02} , Fe ⁺³ _{0.01})(Si _{1.89} , Al _{0.09})O ₃ (OH _{3.98} , Cl _{0.01})
	σ	2.30	3.37	0.70	0.73	0.11	0.04	0.02	0.03	0.02	n.a.	0.00	n.a.	n.a.	0.01	0.10	4.03	0.09	0.21	0.03	0.04	0.01	0.00	0.00	0.00	n.a.	0.00	0.01	0.01	0.01	0.17	13.66	0.02	0.10						
	Min.	33.61	29.99	5.51	0.03	0.21	0.00	0.07	0.00	0.00	n.a.	0.00	n.a.	n.a.	0.00	0.07	75.02	1.78	2.36	0.25	0.01	0.00	0.00	0.00	n.a.	0.00	0.01	3.96	8.86	1.12	4.38	0.00	4.86							
	Max.	41.87	42.37	8.57	2.30	0.71	0.17	0.16	0.13	0.07	n.a.	0.00	n.a.	n.a.	0.05	0.46	88.47	2.10	3.12	0.35	0.13	0.03	0.01	0.00	0.00	n.a.	0.00	0.04	3.99	9.23	1.76	55.00	0.06	5.23						
Exp. C2 (N = 28)	Mean	38.34	34.00	6.32	1.18	0.44	0.04	0.09	0.05	0.01	0.00	0.00	0.05	0.01	0.01	0.09	80.57	1.99	2.62	0.27	0.07	0.02	0.00	0.00	0.00	0.00	0.01	0.01	3.99	8.98	1.32	14.28	0.04	4.98	2.98	0.082	90.78	2.89	0.00	(Mg _{0.82} , Fe ⁺² _{0.27} , Al _{0.06} , Ni _{0.02} , Fe ⁺³ _{0.01})(Si _{1.89} , Al _{0.13})O ₃ (OH _{3.99} , Cl _{0.01})
	Median	38.51	33.26	6.25	1.00	0.42	0.03	0.09	0.04	0.01	0.00	0.00	0.05	0.01	0.01	0.09	79.88	2.02	2.57	0.27	0.06	0.02	0.00	0.00	0.00	0.00	0.01	0.01	3.99	8.95	1.27	8.57	0.03	4.95	2.92	0.098	91.59	13.12	0.00	(Mg _{0.87} , Fe ⁺² _{0.24} , Al _{0.06} , Ni _{0.02} , Fe ⁺³ _{0.01})(Si _{1.89} , Al _{0.13})O ₃ (OH _{3.99} , Cl _{0.01})
	σ	1.44	3.35	0.32	0.60	0.07	0.04	0.02	0.03	0.01	0.01	0.00	0.04	0.03	0.01	0.03	3.48	0.07	0.18	0.01	0.04	0.00	0.00	0.00	0.00	0.00	0.00	0.00	0.00	0.00	0.00	0.08	0.14	17.16	0.02	0.08				
	Min.	34.17	29.09	5.83	0.48	0.33	0.00	0.05	0.00	0.00	0.00	0.00	0.03	0.00	0.03	0.03	75.74	1.84	2.29	0.25	0.03	0.01	0.00	0.00	0.00	0.00	0.00	0.00	0.00	0.00	0.00	0.00	0.00	0.00	0.00	0.00	0.00	0.00		
	Max.	40.30	41.31	6.98	0.61	0.17	0.12	0.10	0.04	0.01	0.00	0.00	0.16	0.04	0.01	0.16	89.58	2.06	2.99	0.30	0.17	0.03	0.01	0.00	0.00	0.00	0.00	0.01	0.01	4.00	9.15	1.62	65.00	0.08	5.15					
Exp. C2R (N = 15) REPLIC A	Mean	37.60	35.03	6.67	1.30	0.38	0.02	0.09	0.08	0.02	n.a.	0.00	n.a.	n.a.	0.09	0.11	81.40	1.94	2.69	0.29	0.08	0.02	0.00	0.00	0.00	n.a.	0.00	0.												

ANEXO B - Tabela 2: Enstatite-derived serpentine EMPA from both experimental pressures sets.

Oxide wt%

Nb of Ions = Number of ions considering 7 Oxigens per formula unit; t.o.c. = Total octahedral cations ; Σ cations+3 = Sum of trivalent cations ; Mg# = Mg/(Mg+Fe2+); * for the calculated formula ; n.a. = Not available ; Serp-opx = orthopyroxene-derived serpentine

ANEXO C - Tabela 3. Normalized whole-rock XRF of starting peridotite and serpentinized experimental products.

Oxide wt% / Sample	Peridotite PM23	Low Pressure Series (13.4 MPa)					High Pressure Series (20.7 MPa)				
		Exp. A	Exp. B	Exp. C	Exp. D	Exp. A2	Exp. B2	Exp. C2	Exp. C2R	Exp. D2	
SiO ₂	43.43	43.48	43.15	42.75	42.61	43.31	43.18	42.86	42.83	42.27	
MgO	44.01	43.62	42.98	43.02	40.95	44.14	43.82	43.90	43.87	43.97	
Fe ₂ O ₃	8.28	8.17	8.07	8.09	8.56	8.23	8.20	8.17	8.16	8.26	
Al ₂ O ₃	1.92	1.96	1.98	2.04	2.99	1.90	1.93	1.97	1.91	1.83	
CaO	1.51	1.50	1.55	1.67	1.23	1.53	1.60	1.55	1.49	1.52	
TiO ₂	0.07	0.09	0.07	0.07	0.10	0.07	0.07	0.07	0.08	0.09	
MnO	0.11	0.10	0.11	0.11	0.13	0.11	0.11	0.11	0.11	0.11	
NiO	0.30	0.28	0.30	0.26	0.30	0.28	0.28	0.29	0.29	0.29	
Cr ₂ O ₃	0.38	0.37	0.38	0.38	0.39	0.38	0.38	0.38	0.37	0.38	
LOI	0.00	0.43	1.42	1.61	2.74	0.05	0.43	0.71	0.89	1.27	
Total	100.00	100.00	100.00	100.00	100.00	100.00	100.00	100.00	100.00	100.00	
MgO/SiO ₂	1.01	1.00	1.00	1.01	0.96	1.02	1.01	1.02	1.02	1.04	
Al ₂ O ₃ /SiO ₂	0.04	0.05	0.05	0.05	0.07	0.04	0.04	0.05	0.04	0.04	
NiO/Cr ₂ O ₃	0.80	0.75	0.79	0.70	0.78	0.74	0.72	0.75	0.77	0.77	

K₂O, Na₂O and P₂O₅ were always below the detection limits. Fe₂O₃ as total iron.

ANEXO D - Tabela 4: Fluid chemistry evolution and gas analyses of experimental products. Analyses of serpentinization-derived hydrothermal fluids from the Lost City Field and experimental lake waters precipitating Mg-silicates and spherulites are shown for comparison.

This Study		Sample	pH _{25°C}	ICP-OES			Ionic chromatography Cl (mmol/kg)	Gas chromatography (n = 5 for each reported value)					
				Si µmol/kg		Ca (mmol/kg) Fe (µmol/kg) Mg (mmol/kg)		CH ₄ (ppm)	CO ₂ (ppm)	H ₂ (ppm)			
				HNO ₃	Deionized water	ppm/g _{rock}							
Low Pressure Series	Starting Solution*	Starting Solution*	6.0 ± 0.1	-	0.11 ± 0.00	<0.0002	<0.04	<0.0001	545.52 ± 8.23	-	-	-	-
		Exp. A	9.3 ± 0.1	265.75 ± 11.35	226.36 ± 8.16	0.40 ± 0.004	39.28 ± 0.89	0.40 ± 0.03	521.09 ± 10.67	-	-	-	-
		Exp. C	11.0 ± 0.1	26.61 ± 0.35	25.19 ± 1.49	0.31 ± 0.002	<0.04	<0.0001	512.25 ± 7.45	-	-	-	-
		Exp. D	11.3 ± 0.1	13.84 ± 3.19	9.58 ± 0.11	0.36 ± 0.001	<0.04	<0.0001	545.05 ± 13.26	-	-	-	-
	High Pressure Series	Exp. A2	9.3 ± 0.1	194.79 ± 5.68	197.27 ± 2.13	0.49 ± 0.006	<0.04	<0.0001	601.93 ± 14.59	-	-	-	-
		Exp. B2	10.0 ± 0.1	177.4 ± 1.06	188.40 ± 0.71	1.22 ± 0.012	<0.04	<0.0001	-	6.52 ± 0.43	0.47	11.76 ± 2.85	n.d.
		Exp. C2	10.2 ± 0.1	113.89 ± 11.35	98.99 ± 0.35	0.58 ± 0.005	<0.04	<0.0001	567.60 ± 2.42	12.48 ± 1.10	0.89	24.32 ± 18.28	n.d.
		Exp. C2R (REPLICА)	10.5 ± 0.1	57.83 ± 0.35	56.77 ± 0.11	1.20 ± 0.011	<0.04	<0.0001	-	5.31 ± 1.37	0.38	2.18 ± 4.87	n.d.
		Exp. D2	10.7 ± 0.1	91.54 ± 1.77	83.38 ± 0.35	0.70 ± 0.006	<0.04	<0.0001	577.69 ± 13.12	39.83 ± 0.04	2.84	322.13 ± 28.34	98.15 ± 13.28
Seyfried et al. 2015	Lost City Hydrothermal Field	M6 (End member)	10.5 ± 0.05	24.2	26.6	n.a.	1.3	541	1.20 mmol/kg CH _{4(aq)}	n.a.	9.9 mmol/kg H _{2(aq)}		
		BH (End member)	10.6 ± 0.05	72.7	27.4	n.a.	0.0	541	1.26 mmol/kg CH _{4(aq)}	n.a.	10.8 mmol/kg H _{2(aq)}		
		BH (J2-361 CGT-Wu)	10.5 ± 0.05	92.1	26.5	1.7	2.4	543	1.24 mmol/kg CH _{4(aq)}	n.a.	10.5 mmol/kg H _{2(aq)}		
Tutolo & Tosca 2018	Experimental data	Pre-salt alkaline Lake water ¹	10.0-10.5	2300-6100**	~0.5-1.0	n.a.	1.0-2.0	n.a.	n.a.	n.a.	n.a.		

Al, Cr, Mn and Ni measured by ICP-OES in all samples were always below detection limits of 3.70×10^{-5} , 7.69×10^{-4} , 1.82×10^{-5} and 6.81×10^{-6} mmol/kg, respectively. Si concentration was measured by diluting sub-samples with HNO₃ or deionized water. *Prepared by adding 0.56 mol NaCl to deionized water; **Highly supersaturated; ¹Simultaneously precipitating spheroidal CaCO₃ and Mg-silicates under room conditions. "-" = not measured ; n.a. = not available ; n.d. = not detected

ANEXO E – Goldschmidt 2019, Section 3F - Abstract

Progressive silica depletion during experimental serpentinization of peridotite mantle xenoliths

Y. M. PORTELLA^{1,2*}, R. V. CONCEIÇÃO¹, T. A. SIQUEIRA³, D. G. CEDEÑO¹, R. S. IGLESIAS³

¹ Programa de Pós-Graduação em Geociências (PPGGeo), UFRGS, Porto Alegre, Brazil (*correspondence:
ymportella@gmail.com; rommulo.conceicao@ufrgs.br;
daniel.grings@ufrgs.br)

² E&P, Petrobras S.A., Rio de Janeiro, Brazil

³ Instituto do Petróleo e dos Recursos Naturais, PUC-RS, Porto Alegre, Brazil (tiago.siqueira@pucrs.br;
rodrigo.iglesias@pucrs.br)

In the past few years serpentinization reactions have been the focus of many experimental studies aimed mostly at hydrogen and methane production [1–3]. However, such studies have only marginally approached aqueous silica release into the derived fluids, and results are ambiguous. In order to estimate silica depletion during progressive serpentinization, replicate batch experiments of powdered peridotite mantle xenoliths with seawater-salinity brines were conducted at 230°C and 13.5 MPa in different run-times. Water to rock mass ratio (W/R) was kept constant, in agreement with lower range estimates of serpentinization in the Mid-Atlantic ridge [4].

X-ray fluorescence (XRF) and diffraction (XRD) of the products indicates that bulk rock SiO₂ concentration drops continuously from 44.44 to 41.67 wt%, while lizardite precipitates. XRD analyses also suggests that lizardite is the main secondary phase and that no detectable amounts of magnetite or brucite were formed. Under 6 weeks of reaction, silica depletion reaches -6.2% of the original silica content, at an average rate of approximately -0.157% [SiO₂].day⁻¹.

Our results differ from those of [2,3] which reported an initial increase in aqueous silica that was followed by a progressive concentration decrease in the reacted fluid. Bulk rock XRF analysis of the reacted powder implies that SiO₂ depletion in the serpentinized peridotite must be accompanied by progressive increase in aqueous silica concentration in the fluid until saturation. Likewise, XRD analyses indicates that lizardite is the dominant serpentine polymorph, coherent with low temperature (<300°C) serpentinites [5].

- [1] Lazar *et al.* (2012) *Chem. Geol.* **326-327**, 102-112 [2]
Klein *et al.* (2015) *Am. Mineral.* **100**, 991-1002 [3]
McCollom *et al.* (2016) *Geochim. Cosmochim. Acta* **181**, 175-200 [4] Vilis *et al.* (2009) *EPSL* **286**, 414-425 [5] Evans (2004) *Int. Geol. Rev.* **46**, 473–506.

ANEXO F – Portella et al. 2019 (Minerals)

Open Access Communication

First Detection of Methane within Chromitites of an Archean-Paleoproterozoic Greenstone Belt in Brazil

by  **Yuri de Melo Portella**^{1,2,*}   **Federica Zaccarini**³ and   **Giuseppe Etiope**⁴

¹ Programa de Pós-Graduação em Geociências (PPGGeo), Universidade Federal do Rio Grande do Sul (UFRGS), Av. Bento Gonçalves, 9500, Porto Alegre, RS 91501-970, Brazil

² Exploration, Petrobras S.A., Av. República do Chile, 330, Rio de Janeiro, RJ 20031-170, Brazil

³ Department Angewandte Geowissenschaften und Geophysik, Montanuniversität Leoben, Peter Tunner Str. 5, A-8700 Leoben, Austria

⁴ Istituto Nazionale di Geofisica e Vulcanologia, Sezione Roma 2, via V. Murata 605, 00143 Roma, Italy

* Author to whom correspondence should be addressed.

Minerals **2019**, *9*(5), 256; <https://doi.org/10.3390/min9050256>

Received: 5 April 2019 / Revised: 24 April 2019 / Accepted: 26 April 2019 / Published: 29 April 2019

(This article belongs to the Special Issue **Spinel Group Minerals**)

[View Full-Text](#)

[Download PDF](#)

[Browse Figures](#)

Abstract

Abiotic methane is widely documented in seeps, springs and aquifers associated with mafic-ultramafic rocks in Phanerozoic ophiolites, peridotite massifs and intrusions worldwide. Chromitites in ophiolites, in particular, have been interpreted as the rocks potentially generating methane through CO_2 hydrogenation. Here, we document, for the first time, the presence of methane within chromitites in South America. We analyzed, through milling and gas extraction, the content of gas occluded in Cedrolina chromitite samples, belonging to the Pilar de Goiás greenstone belt in Brazil. The chromitites display significant gas concentrations up to $0.31 \mu\text{g CH}_4/\text{g}_{\text{rock}}$ and 2800 ppmv of hydrogen, while the host talc schist is devoid of gas. Stable C isotope composition of methane ($\delta^{13}\text{C}$ from -30 to $-39.2\text{\textperthousand}$) and the absence of organic-matter rich metasediments in the region suggest an abiotic origin. Hydrogen and methane concentrations appear related to high-Cr chromite modal content and to the presence of Ni-sulfides/alloys, which are potential catalysts of CO_2 hydrogenation at temperatures above 200°C . Accessory ruthenium-bearing minerals occurring in the chromitites could also act as catalysts, even at lower temperatures. Geothermometry of chlorite found in the chromitites constrains serpentinization at $\sim 250^\circ\text{C}$, during lower greenschist facies retrograde metamorphism. Hydrogen could be autochthonous, and thus formed under similar temperature, which we hypothesize represents the upper limit for abiotic methane generation in the area (250°C). The Cedrolina chromitites are the first example of CH_4 occurrence in ultramafic rocks related to an Archean-Paleoproterozoic greenstone belt. This may imply that serpentinized Cr-rich chromitites could have been sources of methane for the early Earth's atmosphere. [View Full-Text](#)

Keywords: chromite; catalysts; Ni-sulfides; Ni-Fe alloys; abiotic methanogenesis; serpentinization; hydrogen; chlorite geothermometry; Pilar de Goiás greenstone belt

Link for download:

<https://www.mdpi.com/2075-163X/9/5/256>

DOI:

<https://doi.org/10.3390/min9050256>

ANEXO I

Título da Dissertação/Tese:

“O ELO ENTRE A SERPENTINIZAÇÃO, TRANSPORTE DE SÍLICA, CARBONATOS E SEDIMENTAÇÃO RIFT”

Área de Concentração: Geoquímica

Autor: **Yuri De Melo Portella**

Orientador: Prof. Dr. Rommulo Vieira Conceição

Examinador: Dr. Peter Szatmari

Data: 5 de maio de 2020

Conceito: Excelente

PARECER:

A dissertação manifesta bons conhecimentos físico-químicos, familiaridade com a sequência pré-sal e sal na Bacia de Santos e suas interpretações, permitindo relacioná-las criativamente com os resultados de serpentinização experimental. O candidato, seguindo seu orientador, demonstrou perseverança nos experimentos que levaram-no a construir um modelo alternativo de origem das fácies pré-sal.

ANEXO I

Título da Dissertação/Tese:

"O ELO ENTRE A SERPENTINIZAÇÃO, TRANSPORTE DE SÍLICA, CARBONATOS E SEDIMENTAÇÃO RIFT"

Área de Concentração: Geoquímica

Autor: **Yuri De Melo Portella**

Orientador: Prof. Dr. Rommulo Vieira Conceição

Examinadora: Profa. Dra. Carla Cristine Porcher

Data: A

Conceito:

PARECER:

A dissertação de Yuri de Mello Portella apresenta estudo baseado em petrologia experimental do processo de serpentinização de peridotito com água salina, visando simular as condições desse processo de manto litosférico durante o estiramento de margens continentais. Esse processo pode ter sido observado em diversos contextos de fragmentação continental, incluindo o desenvolvimento da margem brasileira durante a formação de reservatórios carbonáticos de petróleo da província cretássica pré-sal, de modo que as conclusões do trabalho podem ter grande implicações para os modelos prospectivos do mesmo. A monografia está dividida em duas partes. A primeira apresenta breve revisão sobre o processo de serpentinização experimental e o contexto geológico da província pré-sal do Atlântico Sul. Essa parte do texto, embora bem escrita e contendo os elementos necessário para suportar os resultados obtidos no trabalho, poderia ter sido um pouco mais desenvolvida. A segunda parte consiste do artigo internacional submetido a Nature Geosciences, conforme comprovante enviado ao PPGGEO, dessa forma atendendo as normas do programa. O artigo está bem escrito e apresenta resultados consistentes sobre a possibilidade do processo de serpentinização do manto litosférico durante o estiramento de margens continentais terem contribuído com a formação da assembleia de argila minerais magnesianos - carbonato típicos do reservatório do pré-sal, bem como para a formação de hidrocarbonetos com a partir de fonte mantélica e dos depósitos de sal pelo envolvimento da água salina na serpentinização. A conclusão é ousada, mas está em acordo com outros autores que tem sugerido que o clima pode não ser ao menos a única explicação para o desenvolvimento dessas assembleias. Traz também uma sugestão de implicações para a evolução da vida no Arqueano, sugerindo que o processo de serpentinização proposto deve ter sido operente durante o ciclo de formação de supercontinentes. Dois pontos que poderiam ser melhorados são o título da dissertação, que ficou muito genérico e a discussão apresentada no artigo, principalmente no item "Understanding serpentinization in two steps" que ficou um pouco confusa. A dissertação apresentada no meu ponto de vista, traz uma grande contribuição ao pensamento da formação de reservatórios carbonáticos de petróleo da província cretássica pré-sal que permitirá

a formulação de novos modelos científicos e prospectivos.



Assinatura:

Data: 29/03/2020

Ciente do Orientador:

Ciente do Aluno:

ANEX I

Title of the Thesis/Dissertation:

**"O ELO ENTRE A SERPENTINIZAÇÃO, TRANSPORTE DE SÍLICA,
CARBONATOS E SEDIMENTAÇÃO RIFT"****"The link of serpentinization, silica transport, carbonates and sedimentation
in rift environment"**

Area of Concentration: Geochemistry

Author: **Yuri De Melo Portella**

Advisor: Dr Rommulo Vieira Conceição

Examiner: Dr. Stephen Foley

Date: (Day/Month/Year)

Degree: (A, B, C or D). B

Observations:

This thesis is on a theme about which I have little background. It concerns the breakdown of serpentine in hydrothermal situations at (for me) low temperature (230°C) and pressure (<21 MPa). It is relevant to diagenesis and lake compositions in rift environments, and was designed specifically to address processes during the initial breakup of the South Atlantic that led to carbonate-hosted hydrocarbon deposits.

The most important aspect of this scenario is that intense faulting is believed to have facilitated fluid circulation and alteration, resulting in widespread serpentinization of ultramafic rocks lying beneath the sediments. The thesis presents experimental results that show that hydrothermal fluids increase greatly in alkalinity during serpentinization, resulting in the mobilisation of Ca, but not Al, Cr, Ni and Mn.

The standard of logical scientific thought throughout the thesis is very good, and the results are extrapolated well to natural conditions and settings. The analytical methods are wide-ranging and seem internally consistent. For example, the initial and final compositions of serpentines derived from olivine and orthopyroxene seem logical, converging with time to a stoichiometry determined by serpentine.

Magnetite is not observed in the experiments, which is a major difference to widespread serpentinization in mantle rocks. This leads the candidate to propose a two-stage process for which his experiments are almost wholly limited in time to the first stage. As the experiments show serpentinization to be a geologically essentially instantaneous process, it is logical that the process would proceed rapidly to magnetite formation in almost all natural circumstances. This allows the candidate to make conclusions about minerals and fluids that are not observed directly in the experimental results, in which he shows an advanced aptitude for scientific thinking. I like the style of the closing thought on the Archean, which paves the way for future

studies.

The organisation of the thesis did not present the information in the order I would have liked, but it is possible that this was fit to a journal format that the thesis is to be submitted to. After a short introduction, we are thrown straight into results on page 27. At this point the experimental methodology has not even been briefly mentioned, which makes it unclear how the results are to be read. As just two examples of the confusion this causes and questions it raises: (i) what is experiment D shown in the Figure on p.29, and (ii) the loss of SiO₂ described on p.38 makes no sense if this is a closed system experiment, but we have not been told at this stage anything about the experiments (other than P and T).

The methods finally are presented at the end of the thesis, but all of my questions were not answered by them, mostly because I am not familiar with the Hastelloy pressure vessel. The pressure range chosen appears to correspond to depths of just 400-600m, which would appear too low to adequately model the serpentinization, as mantle rocks are usually expected to be at least 10 times deeper. Are higher-pressure experiments perhaps not possible in this apparatus? If so, then some discussion of the potential effects of this large pressure difference could be expected. The application of the results is not helped by Figure 13 being "not to scale", which circumvents this question rather than answers it. The results appear to identify a pressure effect, so that ten times more pressure might slow serpentinization much more. However, I am not sure about the action of a pressure effect in natural rocks, as it is ascribed to compression of the powder: natural rocks do not consist of powder.

Another (minor) point concerning presentation: one or two of the figures could more usefully have been presented in a different format (e.g. Figs 1, 9) to improve legibility of small fonts.

The candidate has produced an abstract at the Goldschmidt Conference and a paper in the journal "Minerals", which is excellent productivity for a Masters student. The results are thought provoking and the work is well done; the only issues for me lie in the presentation and explanations.

As a parting thought, I was reminded by the results about colleagues' work on desilication of mantle rocks at Mt Carmel in Israel, which they hypothesize are due to flushing by reduced fluids. It might be worth seeking applications there, although there does appear to be a difference in the mobilization (or not) of alumina.



Signature:

Date: 6th April, 2020

Ciente do Orientador:

Ciente do Aluno: